

1 **Effects of Coupling a Stochastic Convective Parameterization**
2 **with Zhang-McFarlane Scheme on Precipitation Simulation in**
3 **the DOE E3SMv1.0 Atmosphere Model**

4
5 Yong Wang¹, Guang J. Zhang^{2*}, Shaocheng Xie³, Wuyin Lin⁴, George C. Craig⁵, Qi Tang³, Hsi-
6 Yen Ma³

7
8 ¹Ministry of Education Key Laboratory for Earth System Modeling & Department of Earth
9 System Science, Tsinghua University, Beijing, 100084 China

10 ²Scripps Institution of Oceanography, La Jolla, CA, USA

11 ³Lawrence Livermore National Laboratory, CA, USA

12 ⁴Brookhaven National Laboratory, Upton, NY, USA

13 ⁵Meteorologisches Institut, Ludwig-Maximilians-Universität, Munich, Germany

14
15
16
17
18
19
20 Submitted to *GMD*

21 July 28, 2020

22 Revised Feb 5, 2021

23 *Corresponding author:* Guang J. Zhang (gzhang@ucsd.edu), Scripps Institution of
24 Oceanography, University of California San Diego, La Jolla, CA 92093.

26 **Abstract.** A stochastic deep convection parameterization is implemented into the U.S.
27 Department of Energy (DOE) Energy Exascale Earth System Model (E3SM) Atmosphere Model
28 version 1.0 (EAMv1). This study evaluates its performance on the precipitation simulation.
29 Compared to the default model, the probability distribution function (PDF) of rainfall intensity in
30 the new simulation is greatly improved. Especially, the well-known problem of “too much light
31 rain and too little heavy rain” is alleviated over the tropics. As a result, the contribution from
32 different rain rates to the total precipitation amount is shifted toward heavier rain. The less
33 frequent occurrence of convection contributes to the suppressed light rain, while both more
34 intense large-scale and convective precipitation contribute to the enhanced heavy total rain. The
35 synoptic and intraseasonal variabilities of precipitation are enhanced as well to be closer to
36 observations. ~~The A-sensitivity of the rainfall intensity PDF to the model vertical resolution is~~
37 ~~identified and explained~~ examined. in terms of T the relationships between ~~convective-~~
38 precipitation and ~~dilute~~ convective available potential energy ~~(CAPE)~~ in the stochastic
39 simulation is closer to agrees better with that in the Atmospheric Radiation Measurement (ARM)
40 observations compared with the standard model simulation and between large-scale precipitation
41 and resolved-scale upward moisture flux. The annual mean precipitation is largely unchanged
42 with the use of the stochastic scheme except over the tropical western Pacific, where a moderate
43 increase in precipitation represents a slight improvement. The responses of precipitation and its
44 extremes to climate warming are similar with or without the stochastic deep convection scheme.
45

46 **1. Introduction**

47 Precipitation plays a vital role in the Earth’s climate: the latent heat released during
48 precipitation formation is a major energy source that drives the atmospheric circulation, and ~~the~~
49 precipitation is an important part of the Earth’s hydrological cycle. The accurate simulation of
50 precipitation in global climate models (GCMs) is of great scientific and societal interest.
51 However, GCMs used for current climate simulation and future projections suffer from many
52 biases in the global distribution, frequency and intensity of simulated precipitation (Dai, 2006),
53 which have negatively impacted the model’s fidelity. Rainfall in nature is tightly associated with
54 many complex dynamic and physical processes in the atmosphere, including large-scale
55 circulation, convection, cloud microphysics, and planetary boundary layer (PBL) processes. The
56 deficiencies in representing these processes in GCMs are prime culprits for errors in simulated
57 rainfall (Watson et al., 2017).

58 Among the physical processes in GCMs, the parameterization of convection is responsible
59 for some well-known biases: the double Intertropical Convergence Zone (Zhang and Wang 2006;
60 Zhang et al., 2019), too weak synoptic and intraseasonal variabilities in the tropics (Zhang and
61 Mu, 2005a; Watson et al., 2017), the wrong diurnal cycle of rainfall (Xie et al., 2019), “too much
62 light rain and too little heavy rain” (Dai, 2006; Zhang and Mu, 2005b; O’Gorman and Schneider,
63 2009), to name a few. The conventional deterministic convective parameterization in GCMs
64 represents the ensemble effects of subgrid-scale convective clouds in a model grid box on
65 resolved scale variables. However, in reality, a given grid-scale state may lead to different
66 realizations of subgrid-scale convection (Davies et al., 2013; Peters et al., 2013) rather than to a
67 single “ensemble-mean” response. For instance, two model grid boxes, both in a similar
68 convective-equilibrium state, can have different numbers and/or sizes of convective clouds due
69 to stochasticity (Cohen and Craig, 2006). This stochasticity will appear more frequently as the
70 model grid-box size becomes smaller (Jones and Randall, 2011). Not including stochasticity in
71 convective schemes has been suggested to be at least partly responsible for the weak
72 intraseasonal variability and “too much light rain and too little heavy rain” in GCMs (Lin and
73 Neelin 2000, Wang et al., 2016; Watson et al., 2017; Peters et al., 2017).

74 As suggested in Palmer (2001, 2012), more realistic statistics of the impacts of subgrid
75 convective clouds should be derived by simulating them as random samples from probability
76 distributions conditioned on the grid-scale state, so that the influences of different individual
77 realizations are introduced in the convection parameterization. In this regard, much effort in the

78 past two decades has been made to develop stochastic convection schemes (e.g., Lin and Neelin,
79 2000, 2002; Plant and Craig, 2008; Khouider et al., 2010; Sakradzija et al., 2015). Among these
80 schemes, Plant and Craig (2008) (PC08 hereafter) developed a stochastic deep convection
81 parameterization under a framework based on statistical mechanics (Cohen and Craig, 2006;
82 Craig and Cohen, 2006) for noninteracting convective clouds in statistical equilibrium using
83 cloud-resolving model (CRM) simulations. This scheme was applied to numerical weather
84 prediction (NWP) models and to a GCM in an aquaplanet setting, resulting in some substantial
85 improvements in precipitation simulation (Groenemeijer and Craig, 2012; Keane et al., 2014,
86 2016).

87 Wang et al. (2016) incorporated the PC08 stochastic deep convection scheme into the
88 Zhang-McFarlane (ZM) deterministic deep convection scheme (Zhang and McFarlane, 1995) in
89 the National Center for Atmospheric Research (NCAR) Community Atmosphere Model version
90 5 (CAM5). They found that the introduction of the stochastic scheme improved the simulation of
91 precipitation intensity and intraseasonal variability over the tropics in CAM5 (Wang and Zhang
92 2016; Wang et al., 2017).

93 In this study, we implement the PC08 stochastic deep convection parameterization scheme
94 into the DOE Energy Exascale Earth System Model (E3SM) (Golaz et al. 2019) Atmosphere
95 Model version 1.0 (EAMv1) (Rasch et al. 2019; Xie et al. 2018) and examine its effect on
96 precipitation simulation. The EAMv1 is branched out from CAM5 and thus it inherits many
97 model deficiencies from CAM5 as well. Many modifications in physics parameterizations have
98 been made compared to CAM5 (Rasch et al. 2019; Xie et al. 2018). However, some model biases
99 such as weak precipitation intensity persist (Xie et al. 2019). Thus, besides the precipitation
100 metrics explored in our previous studies (Wang et al. 2016, 2017; Wang and Zhang 2016), this
101 study will evaluate precipitation simulation with more systematical metrics. In addition, the
102 responses of precipitation and its extremes to climate warming with the stochastic deep
103 convection scheme will be investigated.

104 The organization of the paper is as follows. Section 2 presents parameterization, model,
105 experimental design, and evaluation data. Section 3 describes results, including variability,
106 frequency, intensity, amounts, duration, mean state, and responses of precipitation and its
107 extremes to climate warming. The sensitivity of the rainfall intensity pdf to vertical resolution
108 and underlying mechanisms are also presented in this section. Summary is given in section 4.
109

110 2. Parameterization, model, experimental design and evaluation data

111 2.1. Stochastic deep convection parameterization

112 The stochastic convective parameterization scheme of PC08 is modified for climate models
113 when incorporating into the ZM deterministic deep convection scheme. The most essential
114 part of the PC08 scheme involves two probability distributions. One is the probability
115 distribution of mass flux of a cloud; it follows the exponential distribution:

$$116 p(m)dm = \frac{1}{\langle m \rangle} e^{-m/\langle m \rangle} dm \quad (1)$$

117 where $\langle m \rangle$ is the mean mass flux of a cloud and is a preset tuning parameter. The integral of the
118 probability density over all values of mass flux is 1, i.e., probability one that every cloud has a
119 mass flux between zero and infinity. The other is the probability of triggering n clouds for a
120 given cloud mass flux in the range between m and $m+dm$ at a given GCM grid box and time step;
121 it is drawn from a Poisson distribution:

$$122 P_{\langle N \rangle}(n) = \frac{\langle N \rangle^n e^{-\langle N \rangle}}{n!} \quad \text{for } n=0, 1, 2, 3, \dots \quad (2)$$

123 where $\langle N \rangle$ is the ensemble mean number of convective clouds in the grid box. Here the sum of
124 the probabilities over all n must equal one, i.e., probability one that some number between zero
125 and infinity of clouds will be triggered with mass flux in this interval. Thus, the average number
126 of clouds with mass flux between m and $m+dm$, $d\bar{n}(m)$, is:

$$127 d\bar{n}(m) = \langle N \rangle p(m)dm = \frac{\langle N \rangle}{\langle m \rangle} e^{-m/\langle m \rangle} dm \quad (3)$$

128 From eqs. (2) and (3), it follows then that for small, $d\bar{n}(m)$ the probability of launching ~~one~~ one
129 convective cloud with mass flux between m and $m+dm$ is given by:

$$130 p_{d\bar{n}(m)}(n = 1) = \frac{\langle N \rangle}{\langle m \rangle} e^{-m/\langle m \rangle} \langle N \rangle dm \quad (4)$$

131 Note that eq. (4) is not a probability density function, but rather the probability of triggering one
132 cloud for a given cloud mass flux interval ($m, m+dm$), knowing that the average number of
133 clouds within this mass flux interval is $d\bar{n}(m)$, where $d\bar{n}(m)$ denotes the average number of
134 clouds with mass flux between m and $m+dm$, $\langle m \rangle$ is the ensemble mean mass flux of a cloud
135 which is a prescribed parameter, and $\langle N \rangle$ is the ensemble mean number of convective clouds in

136 a given GCM grid box ($\langle N \rangle = \langle M \rangle / \langle m \rangle$, with where $\langle M \rangle$ is the ensemble mean total cloud mass
137 flux given by the closure based on the convective quasi-equilibrium assumption in the ZM
138 deterministic parameterization). For each mass flux bin, whether to launch a cloud is determined
139 by comparing the probability $\frac{1}{\langle m \rangle} e^{-\frac{m}{\langle m \rangle}} dm$ from Eq. (1) with a random number uniformly
140 generated between zero and one ~~which, unlike the update frequency of once a day in Wang et al.~~
141 ~~(2016), is updated every 3 days in consideration of computational resources due to finer vertical~~
142 ~~and horizontal resolutions in the EAMv1 (see section 2.2).~~ Then, the sum of mass fluxes
143 generated this way is multiplied by the factor $\langle N \rangle$ to rescale it to the mass flux of all clouds. The
144 product of the total mass flux and the temperature and moisture tendencies from the bulk plume
145 model gives the final temperature and moisture tendencies by the subgrid convective clouds.

146 There are two modifications to the original implementation in the NCAR CAM5. One is the
147 update frequency of random numbers which, unlike the update frequency of once a day in Wang
148 et al. (2016), is updated every 3 days in consideration of computational resources due to finer
149 vertical and horizontal resolutions in the EAMv1 (see section 2.2). For the same reason, the
150 spatial averaging of input quantities (i.e., vertical profiles of temperature and moisture) to the
151 ~~closure stochastic scheme~~ over neighboring grid points used in the original design of PC08 is not
152 performed because it leads to an excessive communication load. One can argue that at a
153 horizontal model resolution of about 110 km in EAMv1, convective quasi-equilibrium
154 approximately holds over some timescale although at individual model timestep it does not.
155 Thus, although spatial averaging is not applied, the temporal trailing averaging over 3 h at each
156 time step is retained in the scheme. Other modifications to the PC08 scheme for incorporation
157 into the ZM scheme in climate models (Wang et al. 2016) are retained. These include:

158 1) The temporally averaged quantities are used to calculate the ensemble mean cloud mass
159 flux ($\langle M \rangle$), which is determined by the ZM scheme. The unsmoothed grid point quantities are
160 still used in the trigger function and the cloud model.

161 2) The root mean squared cloud radius information originally used in PC08 is not needed in
162 our implementation because the ZM scheme does not use cloud radius.

163 3) The ensemble mean mass flux of a cloud $\langle m \rangle$ is set to $1 \times 10^7 \text{ kg s}^{-1}$ following
164 Groenemeijer and Craig (2012).

165 4) The cloud life cycle effect with a factor dt/T (dt is the model time step and T is the
166 constant lifetime parameter) in PC08 is not taken into account because the ZM deterministic
167 parameterization does not consider the life cycle of convection.

168 ~~5) The mass fluxes from all clouds in a GCM grid box generated from eq. (1) are rescaled~~
169 ~~by a factor $\langle N \rangle$ to account for the fact that there can be many clouds in a GCM grid box.~~

170

171 2.2. EAMv1 model

172 The standard configuration of the DOE EAMv1 uses a spectral element dynamical core at [a](#)
173 110-km horizontal resolution on a cubed sphere geometry and a vertical resolution of 72 layers
174 from the surface to 60 km (10 Pa) (Rasch et al. 2019, Xie et al. 2018). The treatment of PBL
175 turbulence, shallow convection, and cloud macrophysics are unified with a simplified third-order
176 turbulence closure parameterization CLUBB (Cloud Layers Unified by Binormals, Golaz et al.,
177 2002; Larson and Golaz, 2005). The deep convection is represented by the ZM scheme. The
178 Morrison and Gettelman (2008) (MG) microphysics scheme is updated to MG2 (Gettelman et
179 al., 2015) with the prediction of rain and changes to ice nucleation and ice microphysics (Wang
180 et al., 2014). A four-mode version of the modal aerosol module (MAM4) (Liu et al., 2016) is used
181 with improvements to aerosol resuspension, aerosol nucleation, scavenging, convective transport
182 and sea spray emissions for including the contribution of marine ecosystems to organic matter
183 (Rasch et al., 2019). A linearized ozone chemistry module (Hsu and Prather, 2009; McLinden et
184 al., 2000) is used to represent stratospheric ozone and its radiative impacts in the stratosphere.
185 Other modifications for model tuning are provided in detail in Xie et al. (2018).

186

187 2.3. Experimental design

188 Six Atmospheric Model Intercomparison Project (AMIP) type simulations are conducted.
189 Four 6-year simulations are forced by prescribed, seasonally varying climatological present-day
190 sea surface temperatures (SSTs) and sea ice extent, recycled yearly (Stone et al., 2018): two with
191 the default deterministic ZM scheme but having 72 and 30 vertical levels respectively (referred
192 to as EAMv1 and EAMv1-30L) and the other two with the stochastic deep convection scheme
193 (referred to as STOCH and STOCH-30L). The simulations with 30 vertical levels are conducted
194 to facilitate the comparison with Wang et al. (2016), in which the vertical resolution of CAM5 is

195 30 levels (see section 3.3). To explore the responses of precipitation and its extremes to climate
196 warming, similar to EAMv1 and STOCH runs, two 3-year simulations in a warmer climate are
197 conducted, in which a composite SST warming pattern derived from the Coupled Model
198 Intercomparison Project Phase 3 (CMIP3) coupled models (referred to as EAMv1-4K and
199 STOCH-4K respectively) is imposed for the boundary condition of the atmosphere. Following
200 Webb et al. (2017), it is a normalized multi-model mean of the sea surface temperature response
201 pattern from 13 CMIP3 atmosphere-ocean general circulation models, representing the change of
202 SST between years 0-20 and 140-160, the time of CO₂ quadrupling in the 1% runs. Before
203 calculating the multi-model ensemble mean, the SST response of each model was divided by its
204 global mean and multiplied by 4K. This guarantees that the pattern information from all models
205 is weighted equally and that the global mean SST forcing is +4K warming. The first year in all
206 simulations is discarded as a spin-up. Information for all experiments is summarized in Table 1.
207

208 **2.4. Evaluation data**

209 For model evaluation, the following datasets are used: The Clouds and the Earth's Radiant
210 Energy System Energy Balanced and Filled (CERES-EBAF) (Loeb et al., 2009) for evaluation of
211 shortwave and longwave cloud radiative forcing; the Interim European Centre for Medium-
212 Range Weather Forecasts Re-Analysis (ERA-Interim) (Simmons et al., 2007) for sea level pressure,
213 zonal wind, relative humidity, specific humidity, and temperature; the European Remote Sensing
214 Satellite Scatterometer (ERS-SCAT) (Bentamy et al., 1999) for surface wind stress; and the Willmott-
215 Matsuura (Willmott) (Willmott & Matsuura, 1995) data for land surface air temperature.

216 The rainfall mean state is evaluated against the Global Precipitation Climatology Project
217 (GPCP) monthly product (version 2.1) at a resolution of 2.5° (Adler et al., 2003; Huffman et al.,
218 2009) while a daily estimate of GPCP version 1.2 at 1° horizontal resolution (GPCP 1DD)
219 (Huffman et al., 2001, 2012) is used for evaluation of precipitation amount distribution. In
220 addition to GPCP, the Xie-Arkin pentad observations at 2.5° resolution (Xie and Arkin, 1996)
221 and the Tropical Rainfall Measuring Mission 3B42 version 7 (TRMM) daily observations at a
222 resolution of 0.25° over (50°S, 50°N) (Huffman et al., 2007) are applied to evaluate the
223 precipitation variance, ~~while the latter~~ The TRMM data are also used in the PDF of rainfall
224 intensity and the rainfall amount distribution. To estimate the uncertainty in the PDF of
225 precipitation intensity in observations, additional daily rainfall products are used. These include
226 which are TAPEER v1.5, GSMAP-NRT-gauges v6.0, PERSIANN CDR v1, CMORPH v1.0,

227 CRT from the Frequent Rainfall Observation on GridS (FROGS) database (Roca et al., 2019)
228 and GPM IMERG v06b (Huffman et al., 20175) are used. –For the rainfall duration evaluation,
229 the TRMM 3B42 v7 3-hourly data is used. To make the comparison consistent between
230 observations and model simulations, the model data with the same output frequency to that in the
231 corresponding observations/reanalysis data are used and all observations/reanalysis data are
232 regridded to the same 1° lat-lon grids as EAMv1. The US Department of Energy Atmospheric
233 Radiation Measurement (ARM) multi-year observations for daily precipitation and dilute
234 convective available potential energy (CAPE) over the Southern Great Plains (SGP) site for the
235 time period of {2004-2018} (Xie et al. 2004) and Green Ocean Amazon (GOAmazon) field
236 campaign (Martin et al. 2016) site for {2014-2015} (Tang et al. 2016) sites are used to evaluate
237 the simulated CAPE vs. total precipitation relationship.

239 3. Results

240 3.1. Intraseasonal and synoptic variability

241 The simulated variability of precipitation is an important aspect of model performance.
242 Here we focus on intraseasonal and synoptic-scale variability. The intraseasonal variability
243 associated with Madden-Julian oscillations (MJO) is problematic in many GCMs (Jiang et al.
244 2015; Zhang and Mu 2005). Figure 1 shows the tropical distribution of the 20-80 day
245 intraseasonal variance for the total precipitation in observations and simulations. The variance is
246 obtained with a Lanczos band-pass filter at each grid point. Both Xie-Arkin and TRMM
247 observations show large variance in the Indian Ocean and western Pacific as well as in the ITCZ
248 and the South Pacific Convergence Zone (SPCZ) regions. The intraseasonal variance in EAMv1
249 is much weaker, as in many other GCMs. Similar to the results in Wang et al. (2016), the
250 STOCH run with the stochastic deep convection scheme has a significantly enhanced
251 intraseasonal variance in these regions, making it much more comparable to observations_
252 although there is excessive precipitation variance over central Africa, the Himalayas, the
253 Maritime Continent and the region near the Colombian coast. Compared with the EAMv1 run,
254 the STOCH run has more small-scale noise in the spatial structure of the precipitation
255 variability.

256 Besides the intraseasonal variance, the synoptic variance (2-9 day Lanczos band pass-
257 filtered rainfall anomalies) is also investigated (Fig. 2). The synoptic-scale variance corresponds
258 to weather activities. In Fig. 2 only TRMM observations are shown to evaluate simulations

259 because the Xie-Arkin observations are pentad data. In TRMM, the geographical distribution of
260 the synoptic variance is similar to that of the intraseasonal variance, but with larger amplitudes
261 because synoptic-scale activities contain much more energy than intraseasonal disturbances.
262 Similar to the intraseasonal variance, the synoptic variance in the EAMv1 run is also much
263 weaker than that in observations. The synoptic-scale variance in the STOCH run is about twice
264 as strong as in EAMv1 although it is still underestimated compared to TRMM observations.
265 Over the regions where the overestimated intraseasonal precipitation variance emerges, the
266 STOCH run has the excessive synoptic precipitation variance as well. This result is consistent
267 with Goswami et al. (2017), which reported enhanced intraseasonal and synoptic variability of
268 precipitation in the National Centers for Environmental Predictions (NCEP) Climate Forecast
269 System version 2 (CFSv2) using a stochastic multcloud model parameterization.-

270

271 **3.2. Rainfall frequency, intensity, amount and duration**

272 Wang et al. (2016) showed that the most significant improvement with the use of the
273 stochastic deep convection scheme in CAM5 was in the simulated PDF of rainfall intensity over
274 the tropics, which became very close to TRMM observations. Since there are many
275 modifications in model configuration and physics parameterizations from CAM5 to EAMv1
276 (Rasch et al. 2019), such as a finer vertical resolution, an updated microphysics parameterization
277 (MG2), and the use of CLUBB in place of separate shallow convection and planetary boundary
278 layer turbulence parameterizations, it is not clear whether a similar degree of improvement in
279 precipitation intensity PDF can be achieved with a similar stochastic convection scheme. Using
280 an equal-interval rainfall intensity bin of 0.5 mm d⁻¹ from 0 to 200 mm d⁻¹, Fig. 3 shows the
281 frequencies of the total precipitation intensity over the tropics (20°S-20°N) from
282 observationsTRMM, EAMv1 and STOCH, respectively. Also shown are the PDFs of large-scale
283 and convective precipitation intensity. The observational uncertainty is larger for intense
284 precipitation than for light precipitation (Fig. 3a), which is consistent with that findings in Roca
285 (2019). The GPCP precipitation intensity distribution (the gray curve that even falls below the
286 EAMv1 curve in Fig. 3a) has the lowest frequency for precipitation intensity greater than 30 mm
287 d⁻¹. The GPCP product whose frequency is even lower than those in EAMv1 is GPCP; it is
288 known to have underestimated precipitation intensities (Kooperman et al., 2016). Despite the
289 uncertainties in observations, the simulated frequencies in STOCH are more consistent with
290 those in the ensemble mean of all observations than those in the default EAMv1. The stochastic

291 convection parameterization in the STOCH run greatly mitigates the bias of “too much light rain
292 and too little heavy rain”, showing a decrease of the frequency of rainfall intensity between 1 and
293 10 mm d⁻¹ and an increase of that of rainfall intensity larger than 20 mm d⁻¹ compared to the
294 EAMv1 run. Especially for light rain, the frequencies in STOCH fall in the observational range
295 while those in EAMv1 do not. ~~The product whose frequency is even lower than those in EAMv1~~
296 ~~is GPCP; it is known to have underestimated precipitation intensities (Kooperman et al.,~~
297 ~~2016).~~ As seen in Fig. 3a, A recent study finds that the decreased frequency of light rain has a
298 profound impact on simulated aerosol loading in the atmosphere (Wang et al. 2021). ~~the~~
299 ~~stochastic convection parameterization in the STOCH run greatly mitigates the bias of “too much~~
300 ~~light rain and too little heavy rain”, showing a decrease of the frequency of rainfall intensity~~
301 ~~between 1 and 10 mm d⁻¹ and an increase of that of rainfall intensity larger than 20 mm d⁻¹~~
302 ~~compared to the EAMv1 run.~~ Xie et al. (2019) indicated that the “too much light rain” in EAMv1
303 was a result of too frequent convection. Consistent with this notion, Fig. 3b shows that the
304 reduction of the light rain frequency is entirely from convective precipitation. On the other hand,
305 the increase of intense precipitation frequency is from both convective and large-scale
306 precipitation.–

307 To understand why the use of stochastic convection scheme decreases the frequency of light
308 rain and increases the frequency of heavy rain, we conducted an additional simulation. In the
309 simulation, the setup is identical to the STOCH run except that the ZM scheme is called a second
310 time at each time step, with input (temperature, moisture, etc.) identical to that for the stochastic
311 scheme. However, the output is used for diagnostic purposes only and does not participate in
312 model integration. It is found that (figure not shown) two factors contribute to the decreased
313 frequency of light rain and increased frequency of heavy rain. First, for a given ensemble mean
314 convective mass flux (from the ZM scheme) the probability for cloud generation following the
315 Poisson distribution for a realization in the stochastic scheme can produce more intense
316 precipitation than obtained by the ZM scheme. Second, the probability distribution results in less
317 frequent convection in general. This allows the buildup of the atmospheric instability (also see
318 Fig. 9 below in section 3.3), which also leads to heavier convective rainfall (even with ZM
319 scheme alone without considering the stochastic part) as well as more large-scale condensation.
320 However, we note that the increase of the frequency in rainfall intensity ranges from 60 to 140
321 mm d⁻¹ in the STOCH run is not as much as that in Wang et al. (2016) for CAM5. This will be
322 elucidated through sensitivity experiments in the next subsection.

323 The frequencies of total precipitation intensity over selected regions also show qualitatively
324 similar degree of improvement. Fig. 4 shows six regions during their convectively active
325 seasons: Amazonia, tropical western Pacific, India for June-September, Maritime Continent,
326 ~~Southern Great Plains (SGP)~~ for May-August and eastern China for June-August in TRMM,
327 EAMv1 and STOCH, respectively. In all tropical regions, the EAMv1 simulation overestimates
328 the occurrence frequency for precipitation intensities less than 20 mm day^{-1} and underestimates it
329 for precipitation intensities greater than 20 mm day^{-1} , similar to the distribution for the entire
330 tropics. In STOCH, the performance in the pdf over Amazonia and Maritime Continent is better
331 than the pdf over the entire tropics. Although the biases of “too much light rain” over India and
332 tropical western Pacific are alleviated by the stochastic deep convection scheme, the bias of “too
333 little heavy rain” remains, particularly over India where large-scale monsoonal dynamics
334 regulate heavy convective rain (Wang et al., 2018). For the two midlatitude convection regions
335 (SGP and eastern China), although there is also noticeable improvement across the precipitation
336 intensity spectrum, it is less significant compared to other regions, possibly because convection
337 in midlatitude land regions is not as prevalent as in the tropics.

338 Figure 5 shows the geographical distributions of precipitation frequency for all
339 precipitation, for precipitation intensities less than 20 mm d^{-1} , and more than 20 mm d^{-1} ,
340 respectively, over the tropics in observations and simulations (days with precipitation intensity
341 less than 1 mm d^{-1} are considered non-precipitating and thus excluded). In TRMM, the
342 occurrence frequency of rainy days ranges from 30 to 70% with the most frequent rain along the
343 ITCZ, the SPCZ and in the Indian Ocean, where the EAMv1 run has as high a frequency as 80-
344 90%, with up to 30% positive biases. In contrast, the STOCH run reduces the frequency to 50-
345 70% although it is still overestimated. When the total precipitation is broken down into
346 precipitation rates less than 20 mm d^{-1} and precipitation rate above 20 mm d^{-1} , in both
347 observations and simulations the geographical distribution of the rainy days is dominated by that
348 of days with precipitation intensity less than 20 mm d^{-1} . In comparison with observations, again,
349 the STOCH run reduces the positive bias of the frequency of precipitation intensity less than 20
350 mm d^{-1} in the EAMv1 run by up to 20%. For precipitation intensities greater than 20 mm d^{-1} , the
351 EAMv1 run underestimates their frequency compared to the TRMM observations. On the other
352 hand, the frequency of occurrence in the STOCH run is comparable to the TRMM observations.

353 Another metric for the precipitation pdf is the contribution of precipitation within a given
354 intensity bin to the total precipitation amount. It combines the information of precipitation

355 frequency distribution and precipitation intensity. While drizzle occurs much more frequently
 356 than the more intense rain events, it may not contribute much to the total precipitation amount.
 357 Following the approach of Kooperman et al. (2016, 2018), we divide the precipitation rate
 358 ranging from 0.1 to 1000 mm d⁻¹ into equal bin intervals on a logarithmic scale, with a bin width
 359 of $\Delta \ln(R) = \Delta R/R = 0.1$. If the frequency of rainfall rates falling into the i th bin is denoted f_i ,
 360 then $f_i = n_i/N_t$, where N_t is the total number of days, n_i is the number of days with rainfall
 361 rates falling into the i th bin. The mean precipitation rate in the i th bin is then:

$$362 \quad R_i = \frac{1}{n_i} \sum_{j=1}^{n_i} r_j, \quad (52)$$

363 where r_j is an individual precipitation rate within the i th bin. Thus, the contribution to the total
 364 precipitation amount from the i th bin per unit bin width is given by:

$$365 \quad P_i = \frac{f_i R_i}{\Delta \ln(R)} = \frac{1}{\Delta \ln(R)} \frac{1}{N_t} \sum_{j=1}^{n_i} r_j \quad (63)$$

366 P_i has the units of mm d⁻¹. The total precipitation amount is then given by:

$$367 \quad P = \sum_i P_i \Delta \ln(R) = \sum_i f_i R_i \quad (74)$$

368 Accordingly, the amount distributions for total (P^T), convective (P^C) and large-scale (P^L)
 369 rainfall are given by:

$$370 \quad P_i^T = \frac{1}{\Delta \ln(R)} \frac{1}{N_t} \sum_{j=1}^{n_i} r_j^T \quad (85)$$

$$371 \quad P_i^C = \frac{1}{\Delta \ln(R)} \frac{1}{N_t} \sum_{j=1}^{n_i} r_j^C \quad (96)$$

$$372 \quad P_i^L = \frac{1}{\Delta \ln(R)} \frac{1}{N_t} \sum_{j=1}^{n_i} r_j^L \quad (107)$$

373 where r^T , r^C and r^L are the total, convective and large-scale rain rates.

374 Figure 6a shows the contribution to the total rainfall amount from each rainfall rate on a
 375 logarithmic scale for GPCP 1DD, TRMM, and the two simulations, respectively, over the
 376 tropics. The TRMM observations have larger contributions from intense rainfall rates than GPCP
 377 1DD, with the peak contribution rainfall rate of 28 mm d⁻¹, higher than the value of 22 mm d⁻¹ in
 378 GPCP 1DD. The EAMv1 run produces a much smaller peak contribution rainfall rate (15 mm d⁻¹)
 379 than the two observations while the STOCH run simulates it realistically (23 mm d⁻¹), falling
 380 in between the two observations. Note that precipitation from intensities less than 1 mm d⁻¹
 381 contributes about 0.05 mm d⁻¹ or less to the tropical mean total precipitation, thus justifying
 382 treating it as non-precipitating in Fig. 5. Fig. 6b shows the convective and large-scale

383 contributions to the simulated total precipitation from EAMv1 and STOCH, respectively. The
384 large-scale precipitation shows very similar contribution distributions in the two simulations,
385 except for the largest rain rates which make only a small contribution to the total. For the most
386 part, large-scale precipitation is not affected by how convection is treated in the model, with both
387 simulations having a maximum contribution near 22 mm d^{-1} . On the other hand, the convective
388 contribution is very different between the two simulations. Similar to the total precipitation, the
389 peak contribution to convective precipitation is at a much smaller rainfall rate in EAMv1 than in
390 STOCH.

391 Besides precipitation frequency and intensity, another important higher order statistic of
392 precipitation is the duration of precipitation events; it measures the intermittency of precipitation
393 (Trenberth et al. 2017). Using 3-hourly data, we calculate the duration of rainfall events as
394 continuous number of hours of precipitation exceeding a threshold value of 1 mm d^{-1} . Figure 7
395 shows the frequency of precipitation events for different durations over the tropics. 80% of
396 TRMM observed precipitation events lasts for 3 hours or less, 18% lasts for 6 hours and 2% lasts
397 for 9 hours. In contrast, both EAMv1 and STOCH produce very small proportions ($\sim 15\%$) of
398 precipitation events that last for 3 hours or less. The frequency of precipitation events lasting 9
399 hours or longer is extremely overestimated in the model simulations, with some lasting for as
400 long as 21 hours. This suggests that convection in the model lacks the observed intermittency
401 (Trenberth et al. 2017) and the use of the stochastic convection scheme does not improve this
402 aspect of the simulated convection.

403

404 **3.3 Sensitivity of rainfall intensity PDF to vertical resolution**

405 A significant modification among several changes in EAMv1 from CAM5 is a much finer
406 vertical resolution, increasing from 30 levels in CAM5 to 72 levels in EAMv1. Within the PBL
407 alone EAMv1 has 17 layers compared to 5 layers in CAM5, and the thickness of approximately
408 20 m for the lowest model layer in EAMv1 is much thinner than that in CAM5, which is 100 m
409 (Xie et al., 2018). The increased resolution in the PBL in EAMv1 will likely affect the
410 convection behavior through PBL-convection interactions. In Fig. 3 we showed that the
411 precipitation intensity pdf is significantly improved with the introduction of the stochastic
412 convection scheme. However, the improvement was not as striking as that shown in Wang et al.
413 (2016) for CAM5. We suspect that this is primarily due to the enhanced vertical resolution in
414 EAMv1 rather than other changes in model physics parameterizations, tunings, or the model

415 dynamic core. To confirm this, EAMv1-30L and STOCH-30L runs with a vertical resolution of
 416 30 layers are conducted and compared with the EAMv1 and STOCH runs with the default 72
 417 vertical layers. As seen in Figure 8, when switching to a configuration of 30 vertical layers, the
 418 performance of the STOCH-30L run is very similar to that in CAM5 (Wang et al., 2016). The
 419 frequency distribution of rainfall intensity between 60 and 140 mm d⁻¹ almost falls on top of that
 420 in TRMM. The PDF of rain intensity in the EAMv1-30L run is also closer to TRMM
 421 observations compared to the EAMv1 run (Fig. 8a). For EAMv1, both convective and large-scale
 422 precipitation becomes more intense in the 30-level configuration. ~~The resolution-dependence
 423 result of large-scale precipitation is described in more detail consistent with the scale analysis
 424 in by Rauscher et al. (2016). In their Equation (2) of Rauscher et al. (2016), there is a term
 425 related to the vertical grid spacing. Once if the terms are rearranged to solve for vertical velocity
 426 (ω), this yields their gives relationship $\omega \propto \Delta p$, the vertical grid-spacing (Δp is pressure
 427 coordinates). Therefore, the result of Rauscher et al., (2016) implies that vertical velocity should
 428 increase as vertical grid spacing increases. With intensified vertical velocity, higher vertical
 429 moisture fluxes are produced for the 30L simulations. Stronger vertical velocity would lead to
 430 more intense precipitation, leading to larger large-scale precipitation. In contrast STOCH-30L,
 431 while the frequency of more intense convective precipitation in STOCH-30L is
 432 increased, the frequency while that of more intense large-scale precipitation is decreased,
 433 probably affected by the moisture depletion from strong convective precipitation (Fig. 8b&c),
 434 similar to the dependence of precipitation pdf on horizontal resolution documented in previous
 435 studies, which showed that refining the horizontal resolution should result in more large-scale
 436 precipitation and less convective precipitation (e.g., O'Brien et al., 2016).~~

437 The causes of ~~the~~ sensitivity of convective ~~and large-scale~~ precipitation to vertical
 438 resolution are further examined below. In the ZM convection scheme, the amount of convection
 439 is linked to ~~dilute convective available potential energy~~ (CAPE ~~(for convenience we will simply
 440 call it CAPE below with the understanding that it refers to dilute CAPE)~~). Thus, in Figure 9 we
 441 present the joint PDF of convective precipitation and ~~dilute~~ CAPE over the tropics in the four
 442 simulations. Note that all parameter settings are identical between EAMv1 and EAMv1-30L
 443 except the vertical resolution. Both EAMv1 and EAMv1-30L show an approximately linear
 444 relationship between ~~dilute~~ CAPE and convective precipitation. ~~The Dilute~~ CAPE values are
 445 generally smaller in EAMv1-30L than in EAMv1, as can be seen from the frequency of
 446 occurrence of both large and medium ~~dilute~~ CAPE values. However, the slope of the maximum

447 occurrence frequency is almost twice as large in EAMv1-30L as in EAMv1 (Fig. 9a&b), giving
448 the higher frequency of larger convective precipitation as seen in Fig. 8. This is because that a
449 coarser vertical resolution means stronger vertical mixing, which results in higher precipitation
450 for given dilute-CAPE values. This result is puzzling to us at first. However, note that Ffor a
451 given precipitation rate that the model produces, there is in general a large range of dilute-CAPE
452 values and the dilute-CAPE values in EAMv1 are predominantly larger than in EAMv1-30L as
453 can be seen from the pdf distribution in Fig. 9a and b. Compared to EAMv1, the smaller dilute-
454 CAPE values in EAMv1-30L are caused by higher parcel launching levels due to thicker model
455 layers near the surface, where the most unstable air is often found (figure not shown). There is
456 also a bifurcation for medium to large dilute-CAPE values. This is likely related to atmospheric
457 moisture conditions in the atmosphere: for the same dilute-CAPE values there is less
458 precipitation when the atmosphere is dry, and vice versa. With the introduction of the stochastic
459 deep convection scheme, there are no longer ~~an~~ approximately linear relations between dilute-
460 CAPE and convective precipitation (Fig. 9c&d) in spite of the fact that the CAPE-based closure
461 is still used to determine the cloud base mass flux (presumably the ensemble mean). This is
462 surprising; it implies that for a given convectively unstable atmospheric thermodynamic
463 condition, the use of the stochastic scheme often inhibits the triggering of convection, thereby
464 allowing for the buildup of dilute-CAPE for (the less frequently occurring) stronger convection.
465 Similar to EAMv1, smaller (larger) dilute-CAPE values occur more (less) frequently in STOCH-
466 30L due to higher parcel launching levels. Also, the small and moderate values of CAPE have
467 larger probabilities to precipitate more in STOCH-30L compared to STOCH.

468
469 Over the ARM SGP and GOAmazon sites, no linear relationship is seen between the total
470 total-precipitation and dilute-CAPE in observations (Fig. 10). At the SGP site, high dilute-CAPE
471 values generally correspond to low total-precipitation. At the GOAmazon site, high total-
472 precipitation values correspond to medium values of dilute-CAPE, somewhat resembling the
473 STOCH simulation, although the observed dilute-CAPE values at the GOAmazon site are much
474 smaller than those in the simulations. Because large-scale precipitation is related to resolved-scale
475 upward moisture flux $\omega q/g$, where ω is vertical velocity in pressure coordinate, q is specific-
476 humidity and g is gravitational acceleration (O'Brien et al., 2016), Fig. 10 shows the PDFs of-
477 upward moisture flux at 850 hPa in the simulations. In comparison with the 72-level
478 configuration, EAMv1-30L has larger frequencies for upward moisture fluxes larger than 20 mm

479 ~~d^+ while STOCH-30L has larger frequencies for upward moisture fluxes from 20 to 80 $mm d^{-1}$ -~~
480 ~~but smaller frequencies for fluxes larger than 80 $mm d^{-1}$. These correspond well with the changes~~
481 ~~in the PDF of large-scale precipitation from the 30-level to the 72-level simulations in Fig. 8.~~

482

483 3.4 Mean state

484 So far, we have shown that the introduction of a stochastic convection scheme into the
485 E3SM atmospheric model can significantly improve the simulation of short-term variability and
486 intensity pdf of precipitation. In climate model development efforts, it is important that an
487 improvement in some aspects of the model does not lead to degradation of other aspects, at least
488 not to outweigh the improvement. Thus, it is imperative that we examine the climate mean fields
489 as well. Fig. 11 shows the global distribution of annual mean precipitation in GPCP observations
490 and simulations, as well as the differences of total, convective, and large-scale precipitation
491 between the STOCH and EAMv1 runs. Overall, the geographical distributions of precipitation in
492 the two simulations are similar to those in observations, but both overestimate the tropical
493 precipitation (Fig. 11a-c). There is a slight increase of rainfall over the tropical western Pacific,
494 equatorial Indian Ocean and Africa and a slight decrease over India and Amazonia in the
495 STOCH simulation (Fig. 11d). Most of these changes are from convective precipitation except
496 over equatorial Africa where the changes are from large-scale precipitation (Fig. 11e&f).

497 The zonal mean of temperature and specific humidity from ERAI and the model biases are
498 shown in Figure 12. For temperature, EAMv1 produces mostly negative biases in the entire
499 troposphere over the tropics and subtropics and positive biases in the lower troposphere in high
500 latitudes. With the stochastic deep convection scheme used, the temperature changes in STOCH
501 are very minor, increasing slightly from EAMv1. In the simulation of specific humidity, there are
502 positive biases in the lower troposphere across all latitudes and negative biases above 900 hPa
503 over the tropics and subtropics in EAMv1. In comparison with EAMv1, the negative biases are
504 alleviated but the positive biases are increased slightly in STOCH.

505 The overall difference in model performance as measured by the commonly used mean
506 climate metrics between EAMv1 and STOCH runs is summarized in the Taylor diagram (Fig.
507 13). Most metrics are comparable between the two simulations except precipitation, especially
508 over land where STOCH shows a larger standard deviation than both GPCP and EAMv1. In
509 short, the mean climate does not change much after the incorporation of the stochastic
510 convection scheme in EAMv1. This is practically desirable since one does not need to heavily re-

511 tune the model, a task that is often time-consuming and more of engineering than scientific
512 interest.

513

514 **3.5. Response to climate warming**

515 Another aspect of interest concerns the model's response to climate change. It is well
516 known that the estimated climate sensitivity for future climate projections is sensitive to changes
517 in model physics parameterizations (Golaz et al. 2019). With the stochastic deep convection
518 parameterization, it is necessary to check if the response of precipitation and associated extremes
519 to climate warming differs. As seen in Fig. 14, relative to the current climate simulations, the
520 geographical patterns and magnitudes of annual mean precipitation changes normalized by the
521 global-mean surface air warming (ΔT_{sa}) in the +4K SST warming simulations (i.e., $(P_{+4k} -$
522 $P)/P/\Delta T_{sa}$, units: %/K) with and without the stochastic deep convection scheme are very
523 similar, both showing maximum increases over the ITCZ, the western Pacific and the Indian
524 Ocean. Pendergrass et al., (2019) found that the response of extreme precipitation to warming
525 follows a nonlinear relation:

$$526 \quad \frac{dr_x}{dT_{sa}} = aT_{sa} \quad (118)$$

527 or

$$528 \quad r_x = \frac{1}{2} aT_{sa}^2 + b \quad (129)$$

529 where r_x is a rainfall extreme index (here using R95p, the total rainfall from the days with daily
530 rainfall intensity exceeding 95th percentile of the daily precipitation distribution), T_{sa} is the
531 global-mean surface air temperature in a warmer world, and a is the slope of dr_x/dT_{sa} versus
532 T_{sa} measuring the strength of the nonlinear response of extreme rainfall to warming. At each
533 grid point, $dr_x \approx \Delta r_x$ is equal to R95p in a warmer world minus that under the current climate
534 and normalized by the global-mean surface air warming ($dT_{sa} \approx \Delta T_{sa}$). With T_{sa} in the +4K
535 SSTs warming simulations and the calculated dr_x/dT_{sa} , the global distributions of the slope, a
536 (units: %/K²), with and without the stochastic deep convection scheme are displayed in Fig.
537 14c&d. Although the stochastic deep convection parameterization introduces stochasticity into
538 convection and significantly improves the underestimated frequency of intense precipitation
539 under the current climate (Wang et al., 2017), it does not lead to a different nonlinear response of
540 precipitation extremes in a warmer world. The resemblance of the coefficient a between the two
541 simulations results from the similar response of the fractional change in r_x to global warming

542 [\(Fig. 14e&f\)](#). Increasing circulation strength as [the](#) climate warms is considered to be the main
543 driver for the nonlinear relationship between tropical precipitation extremes and global-mean
544 surface air temperature (Pendergrass et al., 2019), and it is possible that the circulation changes
545 with and without the stochastic deep convection scheme are similar. Relative to their respective
546 current climate states, the responses of the EAMv1-4K and STOCH-4K runs show similar
547 geographical distributions with comparable maximum nonlinearity over the tropical Pacific and
548 Atlantic and the Indian Ocean which bears some resemblance to that in Pendergrass et al. (2019).

549

550 **4. Summary**

551 In this study, we implemented the stochastic deep convection scheme (Plant and Craig,
552 2008; Wang et al., 2016) into the DOE EAMv1 and investigated its impact on the simulation of
553 precipitation. Several improvements are observed with the use of the stochastic convection
554 scheme: (1) the weak intraseasonal and synoptic-scale variabilities in EAMv1 are enhanced to
555 levels much closer to those in observations; (2) the “too much light rain and too little heavy rain”
556 bias over the tropics is significantly alleviated due to less frequent occurrence of drizzling
557 convection and more frequent occurrence of intense large-scale and convective precipitation
558 contributing to enhanced heavy rain; (3) the simulated peak precipitation rates (the amount
559 mode) in the precipitation amount distribution, which contribute the most to the total amount of
560 precipitation, are larger and are in better agreement with those in TRMM and GPCP
561 observations.

562 While the improvement in the simulated PDF of rainfall intensity is significant, it is less
563 than what we had expected based on our earlier work with the NCAR CAM5 (Wang et al.,
564 2016). Since there are many changes from CAM5 to EAMv1, including vertical resolution,
565 model dynamic core and physics parameterizations, it is not clear which changes are related to
566 the difference in the improvement of the simulated rainfall pdf. Two sensitivity tests were
567 performed to elucidate this, both with a coarser vertical resolution configuration of 30 layers
568 (i.e., EAMv1-30L and SOTC-30L) as in CAM5. The STOCH-30L run successfully reproduces
569 the frequency distribution of rainfall intensity found by Wang et al. (2016) with an increased
570 frequency of convective precipitation intensities between 60 and 140 mm d⁻¹. This increase is
571 explained by the fact that small and moderate values of CAPE generate more convective
572 precipitation from the altered relation between them compared to the 72-level configuration due
573 to fewer model layers in the 30-level resolution. [Following the framework](#)~~Since that vertical~~

574 velocity should in general increase with the as vertical grid spacing increases, the increase of
575 large-scale precipitation also has the contribution to the increased frequency of total
576 precipitation intensities in the 30-level configuration. Large-scale precipitation is also influenced
577 by the vertical resolution, but it behaves differently in EAMv1-30L and STOCH-30L compared
578 with EAMv1 and STOCH respectively because of the different response of the resolved scale
579 upward moisture flux at 850 hPa.

580 For any changes in model physics parameterization that improve some aspects of the model
581 performance, it is important that other aspects are not degraded. It is known in the climate
582 modeling community that improved intraseasonal variability is often accompanied by a
583 degradation of the mean state (e.g., Kim et al. 2011; Klingaman and Demott, 2020). We showed
584 that the mean states in tropospheric temperature, moisture as well as precipitation are not much
585 different with or without the use of the stochastic convection scheme, and neither are the
586 responses of mean precipitation and precipitation extremes to climate warming. This is
587 encouraging and desirable for model development efforts. However, we note that for higher
588 horizontal resolutions (Caldwell et al., 2019) or a regionally refined mesh version of EAMv1
589 (Tang et al., 2019), spatial averaging of the input fields of the stochastic scheme would be
590 needed to make use of convective quasi-equilibrium over a larger domain. This could be
591 challenging for computational efficiency and it requires further research in the future.

592
593 **Code and data availability.** The E3SMv1 source code can be downloaded from the E3SM
594 official website <https://e3sm.org/>. The GPCP 1DD data is available from NASA GSFC RSD
595 (<https://psl.noaa.gov/data/gridded/data.gpcp.html>). and TRMM and GPM3B42 data are
596 available from <https://gpm.nasa.gov/data/directory> available from NASA GSFC RSD
597 (<https://psl.noaa.gov/data/gridded/data.gpcp.html>) and Mirador (<http://mirador.gsfc.nasa.gov>),
598 respectively. The availability of daily precipitation observations from the FROGS database is
599 indicated described in Rocga et al. (2019). The ARM observations over the SGP and
600 GOe Amazon sites are available from <https://www.arm.gov/data>. The EAMv1 simulation output
601 is provided in an open repository Zenodo (<http://doi.org/10.5281/zenodo.3902998>).

602
603 **Author contributions.** GJZ conceived the idea. YW developed the model code. YW and WYL
604 conducted the model simulations. YW performed the analysis. YW and GJZ interpreted the
605 results and wrote the paper. All authors participated in the revision and editing of the paper.

606
607
608
609
610
611
612
613
614
615
616
617
618
619
620
621
622

Acknowledgements: This work is supported by the National Key Research and Development Program of China Grants 2017YFA0604000, and the National Natural Science Foundation of China Grants 41975126 and 41605074. GJZ is supported by the Department of Energy, Office of Science, Biological and Environmental Research Program (BER), under Award Numbers DE-SC0019373 and DE-SC0016504. GCC is supported by subproject A1 of the Transregional Collaborative Research Center SFB / TRR 165 “Waves to Weather” (www.wavestoweather.de) funded by the German Research Foundation (DFG). Work at LLNL was performed under the auspices of the U.S. DOE by Lawrence Livermore National Laboratory under contract No. DE-AC52-07NA27344. SX and QT are supported by the DOE Energy Exascale Earth System Model (E3SM) project and HYM is funded by the DOE Regional and Global Model Analysis program area (RGMA) and ASR’s Cloud-Associated Parameterizations Testbed (CAPT) project. This research used resources of the National Energy Research Scientific Computing Center, a DOE Office of Science User Facility supported by the Office of Science of the U.S. DOE under Contract No. DE-AC02-05CH11231. The authors would like to thank the two anonymous reviewers for their valuable constructive and helpful comments.

623 **References**

624 Adler, R. F., Huffman, G. J., Chang, A., Ferraro, R., Xie, P.-P., Janowiak, J., Rudolf, B.,
625 Schneider, U., Curtis, S., and Bolvin, D.: The version-2 global precipitation climatology
626 project (GPCP) monthly precipitation analysis (1979–present), *Journal of*
627 *hydrometeorology*, 4, 1147-1167, 2003.

628 Bentamy, A., Queffelec, P., Quilfen, Y., and Katsaros, K.: Ocean surface wind fields estimated
629 from satellite active and passive microwave instruments, *IEEE transactions on geoscience*
630 *and remote sensing*, 37, 2469-2486, 1999.

631 Caldwell, P. M., Mametjanov, A., Tang, Q., Van Roekel, L. P., Golaz, J.-C., Lin, W., Bader, D.
632 C., Keen, N. D., Feng, Y., Jacob, R., Maltrud, M. E., Roberts, A. F., Taylor, M. A.,
633 Veneziani, M., Wang, H., Wolfe, J. D., Balaguru, K., Cameron-Smith, P., Dong, L., Klein,
634 S. A., Leung, L. R., Li, H.-Y., Li, Q., Liu, X., Neale, R. B., Pinheiro, M., Qian, Y., Ullrich,
635 P. A., Xie, S., Yang, Y., Zhang, Y., Zhang, K., and Zhou, T.: The DOE E3SM Coupled
636 Model Version 1: Description and Results at High Resolution, *Journal of Advances in*
637 *Modeling Earth Systems*, 11, 4095-4146, 10.1029/2019ms001870, 2019.

638 Cohen, B. G., and Craig, G. C.: Fluctuations in an Equilibrium Convective Ensemble. Part II:
639 Numerical Experiments, *Journal of the Atmospheric Sciences*, 63, 2005-2015,
640 10.1175/JAS3710.1, 2006.

641 Craig, G. C., and Cohen, B. G.: Fluctuations in an Equilibrium Convective Ensemble. Part I:
642 Theoretical Formulation, *Journal of the Atmospheric Sciences*, 63, 1996-2004,
643 10.1175/JAS3709.1, 2006.

644 Dai, A.: Precipitation Characteristics in Eighteen Coupled Climate Models, *Journal of Climate*,
645 19, 4605-4630, 10.1175/JCLI3884.1, 2006.

646 Davies, L., Jakob, C., May, P., Kumar, V. V., and Xie, S.: Relationships between the large-scale
647 atmosphere and the small-scale convective state for Darwin, Australia, *Journal of*
648 *Geophysical Research: Atmospheres*, 118, 5115-5145, 10.1002/jgrd.50645, 2013.

649 Gettelman, A., Morrison, H., Santos, S., Bogenschutz, P., and Caldwell, P.: Advanced two-
650 moment bulk microphysics for global models. Part II: Global model solutions and aerosol-
651 cloud interactions, *Journal of Climate*, 28, 1288-1307, 2015.

652 Golaz, J.-C., Larson, V. E., and Cotton, W. R.: A PDF-based model for boundary layer clouds.
653 Part I: Method and model description, *Journal of the atmospheric sciences*, 59, 3540-3551,
654 2002.

655 Golaz, J.-C., Caldwell, P. M., Van Roekel, L. P., Petersen, M. R., Tang, Q., Wolfe, J. D.,
656 Abeshu, G., Anantharaj, V., Asay-Davis, X. S., Bader, D. C., Baldwin, S. A., Bisht, G.,
657 Bogenschutz, P. A., Branstetter, M., Brunke, M. A., Brus, S. R., Burrows, S. M., Cameron-
658 Smith, P. J., Donahue, A. S., Deakin, M., Easter, R. C., Evans, K. J., Feng, Y., Flanner, M.,
659 Foucar, J. G., Fyke, J. G., Griffin, B. M., Hannay, C., Harrop, B. E., Hoffman, M. J.,
660 Hunke, E. C., Jacob, R. L., Jacobsen, D. W., Jeffery, N., Jones, P. W., Keen, N. D., Klein,
661 S. A., Larson, V. E., Leung, L. R., Li, H.-Y., Lin, W., Lipscomb, W. H., Ma, P.-L.,
662 Mahajan, S., Maltrud, M. E., Mametjanov, A., McClean, J. L., McCoy, R. B., Neale, R. B.,
663 Price, S. F., Qian, Y., Rasch, P. J., Reeves Eyre, J. E. J., Riley, W. J., Ringler, T. D.,
664 Roberts, A. F., Roesler, E. L., Salinger, A. G., Shaheen, Z., Shi, X., Singh, B., Tang, J.,
665 Taylor, M. A., Thornton, P. E., Turner, A. K., Veneziani, M., Wan, H., Wang, H., Wang, S.,
666 Williams, D. N., Wolfram, P. J., Worley, P. H., Xie, S., Yang, Y., Yoon, J.-H., Zelinka, M.
667 D., Zender, C. S., Zeng, X., Zhang, C., Zhang, K., Zhang, Y., Zheng, X., Zhou, T., and Zhu,
668 Q.: The DOE E3SM Coupled Model Version 1: Overview and Evaluation at Standard
669 Resolution, *Journal of Advances in Modeling Earth Systems*, 11, 2089-2129,
670 10.1029/2018ms001603, 2019.

671 Goswami, B., Khouider, B., Phani, R., Mukhopadhyay, P., and Majda, A.: Improving synoptic
672 and intraseasonal variability in CFSv2 via stochastic representation of organized
673 convection, *Geophysical Research Letters*, 44, 1104-1113, 2017.

674 Groenemeijer, P., and Craig, G. C.: Ensemble forecasting with a stochastic convective
675 parametrization based on equilibrium statistics, *Atmos. Chem. Phys.*, 12, 4555-4565,
676 10.5194/acp-12-4555-2012, 2012.

677 Hsu, J., and Prather, M. J.: Stratospheric variability and tropospheric ozone, *Journal of*
678 *Geophysical Research: Atmospheres*, 114, 2009.

679 Huffman, G. J., Adler, R. F., Morrissey, M. M., Bolvin, D. T., Curtis, S., Joyce, R., McGavock,
680 B., and Susskind, J.: Global precipitation at one-degree daily resolution from multisatellite
681 observations, *Journal of hydrometeorology*, 2, 36-50, 2001.

682 Huffman, G. J., Bolvin, D. T., Nelkin, E. J., Wolff, D. B., Adler, R. F., Gu, G., Hong, Y.,
683 Bowman, K. P., and Stocker, E. F.: The TRMM multisatellite precipitation analysis
684 (TMPA): Quasi-global, multiyear, combined-sensor precipitation estimates at fine scales,
685 *Journal of hydrometeorology*, 8, 38-55, 2007.

686 Huffman, G., Bolvin, D., and Adler, R.: GPCP version 1.2 1-degree daily (1DD) precipitation
687 data set, World Data Center A, National Climatic Data Center, Asheville, NC [Available at
688 <ftp://rsd.gsfc.nasa.gov/pub/1dd-v1.2/>], 2012.

689 Huffman, G. J., Bolvin, D. T., and Nelkin, E. J.: Integrated Multi-satellite Retrievals for GPM
690 (IMERG) technical documentation, available at:
691 https://pmm.nasa.gov/sites/default/files/document_files/IMERG_doc.pdf (last access: 8
692 July 2019), 2017.

693 Jones, T. R., and Randall, D. A.: Quantifying the limits of convective parameterizations, *Journal*
694 *of Geophysical Research: Atmospheres*, 116, 10.1029/2010jd014913, 2011.

695 Kain, J. S., and Fritsch, J. M.: A One-Dimensional Entraining/Detraining Plume Model and Its
696 Application in Convective Parameterization, *Journal of the Atmospheric Sciences*, 47,
697 2784-2802, 10.1175/1520-0469(1990)047<2784:AODEPM>2.0.CO;2, 1990.

698 Kain, J. S.: The Kain–Fritsch Convective Parameterization: An Update, *Journal of Applied*
699 *Meteorology*, 43, 170-181, 10.1175/1520-0450(2004)043<0170:TKCPAU>2.0.CO;2, 2004.

700 Keane, R. J., Craig, G. C., Keil, C., and Zängl, G.: The Plant–Craig Stochastic Convection
701 Scheme in ICON and Its Scale Adaptivity, *Journal of the Atmospheric Sciences*, 71, 3404-
702 3415, 10.1175/JAS-D-13-0331.1, 2014.

703 Keane, R. J., Plant, R. S., and Tennant, W. J.: Evaluation of the Plant–Craig stochastic
704 convection scheme (v2.0) in the ensemble forecasting system MOGREPS-R (24 km) based
705 on the Unified Model (v7.3), *Geoscientific Model Development*, 9, 1921-1935, 2016.

706 Khouider, B., Biello, J., and Majda, A. J.: A stochastic multicloud model for tropical convection,
707 187-216, 2010.

708 Kim, D., Sobel, A. H., Maloney, E. D., Frierson, D. M., and Kang, I.-S.: A systematic
709 relationship between intraseasonal variability and mean state bias in AGCM simulations,
710 *Journal of Climate*, 24, 5506-5520, 2011.

711 Klingaman, N. P., and Demott, C. A.: Mean State Biases and Interannual Variability Affect
712 Perceived Sensitivities of the Madden-Julian Oscillation to Air-Sea Coupling, *Journal of*
713 *Advances in Modeling Earth Systems*, 12, e2019MS001799, 10.1029/2019ms001799, 2020.

714 Kooperman, G. J., Pritchard, M. S., Burt, M. A., Branson, M. D., and Randall, D. A.: Robust
715 effects of cloud superparameterization on simulated daily rainfall intensity statistics across
716 multiple versions of the Community Earth System Model, *Journal of Advances in*
717 *Modeling Earth Systems*, 8, 140-165, 2016.

718 Kooperman, G. J., Pritchard, M. S., O'Brien, T. A., and Timmermans, B. W.: Rainfall From
719 Resolved Rather Than Parameterized Processes Better Represents the Present - Day and
720 Climate Change Response of Moderate Rates in the Community Atmosphere Model,
721 Journal of advances in modeling earth systems, 10, 971-988, 2018.

722 Larson, V. E., and Golaz, J.-C.: Using probability density functions to derive consistent closure
723 relationships among higher-order moments, Monthly Weather Review, 133, 1023-1042,
724 2005.

725 Lin, J. W. B., and Neelin, J. D.: Influence of a stochastic moist convective parameterization on
726 tropical climate variability, Geophysical research letters, 27, 3691-3694, 2000.

727 Lin, J. W.-B., and Neelin, J. D.: Considerations for stochastic convective parameterization,
728 Journal of the atmospheric sciences, 59, 959-975, 2002.

729 Liu, X., Ma, P.-L., Wang, H., Tilmes, S., Singh, B., Easter, R., Ghan, S., and Rasch, P.:
730 Description and evaluation of a new four-mode version of the Modal Aerosol Module
731 (MAM4) within version 5.3 of the Community Atmosphere Model, Geoscientific Model
732 Development (Online), 9, 2016.

733 Loeb, N. G., Wielicki, B. A., Doelling, D. R., Smith, G. L., Keyes, D. F., Kato, S., Manalo-
734 Smith, N., and Wong, T.: Toward optimal closure of the Earth's top-of-atmosphere radiation
735 budget, Journal of Climate, 22, 748-766, 2009.

736 [Martin, S. T., Artaxo, P., Machado, L. A. T., Manzi, A. O., Souza, R. A. F., Schumacher, C.,](#)
737 [Wang, J., Andreae, M. O., Barbosa, H. M. J., Fan, J., Fisch, G., Goldstein, A. H., Guenther,](#)
738 [A., Jimenez, J. L., Pöschl, U., Silva -Dias, M. A., Smith, J. N., and Wendisch, M.:](#)
739 [Introduction: Observations and Modeling of the Green Ocean Amazon \(GoAmazon2014/5\),](#)
740 [Atmos. Chem. Phys., 16, 4785–4797, <https://doi.org/10.5194/acp-16-4785-2016>, 2016.](#)

741 McLinden, C., Olsen, S., Hannegan, B., Wild, O., Prather, M., and Sundet, J.: Stratospheric
742 ozone in 3 - D models: A simple chemistry and the cross - tropopause flux, Journal of
743 Geophysical Research: Atmospheres, 105, 14653-14665, 2000.

744 Morrison, H., and Gettelman, A.: A New Two-Moment Bulk Stratiform Cloud Microphysics
745 Scheme in the Community Atmosphere Model, Version 3 (CAM3). Part I: Description and
746 Numerical Tests, Journal of Climate, 21, 3642-3659, 10.1175/2008JCLI2105.1, 2008.

747 ~~[O'Brien, T. A., Collins, W. D., Kashinath, K., Rübél, O., Byna, S., Gu, J., Krishnan, H., and](#)~~
748 ~~[Ullrich, P. A.: Resolution dependence of precipitation statistical fidelity in hindcast simulations,](#)~~
749 ~~[Journal of Advances in Modeling Earth Systems, 8, 976-990, 2016.](#)~~

750 O’Gorman, P. A., and Schneider, T.: The physical basis for increases in precipitation extremes in
751 simulations of 21st-century climate change, *Proceedings of the National Academy of*
752 *Sciences of the United States of America*, 106, 14773-14777, 2009.

753 Palmer, T. N.: A nonlinear dynamical perspective on model error: A proposal for non - local
754 stochastic - dynamic parametrization in weather and climate prediction models, *Quarterly*
755 *Journal of the Royal Meteorological Society*, 127, 279-304, 2001.

756 Palmer, T. N.: Towards the probabilistic Earth-system simulator: a vision for the future of
757 climate and weather prediction†, *Quarterly Journal of the Royal Meteorological Society*,
758 138, 841-861, 2012.

759 Pendergrass, A., Coleman, D., Deser, C., Lehner, F., Rosenbloom, N., and Simpson, I.:
760 Nonlinear response of extreme precipitation to warming in CESM1, *Geophysical Research*
761 *Letters*, 46, 10551-10560, 2019.

762 Peters, K., Jakob, C., Davies, L., Khouider, B., and Majda, A. J.: Stochastic Behavior of Tropical
763 Convection in Observations and a Multicloud Model, *Journal of the Atmospheric Sciences*,
764 70, 3556-3575, 2013.

765 Peters, K., Crueger, T., Jakob, C., and Mobis, B.: Improved MJO - simulation in ECHAM6.3 by
766 coupling a Stochastic Multicloud Model to the convection scheme, *Journal of Advances in*
767 *Modeling Earth Systems*, 9, 193-219, 2017.

768 Plant, R. S., and Craig, G. C.: A Stochastic Parameterization for Deep Convection Based on
769 Equilibrium Statistics, *Journal of the Atmospheric Sciences*, 65, 87-105,
770 10.1175/2007JAS2263.1, 2008.

771 Rasch, P., Xie, S., Ma, P. L., Lin, W., Wang, H., Tang, Q., Burrows, S., Caldwell, P., Zhang, K.,
772 and Easter, R.: An overview of the atmospheric component of the Energy Exascale Earth
773 System Model, *Journal of Advances in Modeling Earth Systems*, 11, 2377-2411, 2019.

774 [Rauscher, S. A., O’Brien, T. A., Piani, C., Coppola, E., Giorgi, F., Collins, W. D., and Lawston,
775 P. M.: A multimodel intercomparison of resolution effects on precipitation: simulations and
776 theory, *Clim Dyn*, 47, 2205-2218, 10.1007/s00382-015-2959-5, 2016.](#)

777 [Roca, R.: Estimation of extreme daily precipitation thermodynamic scaling using gridded satellite
778 precipitation products over tropical land, *Environmental Research Letters*, 14, 095009,
779 10.1088/1748-9326/ab35c6, 2019.](#)

780 [Roca, R., Alexander, L. V., Potter, G., Bador, M., Jucá, R., Contractor, S., Bosilovich, M. G.,
781 and Cloché, S.: FROGS: a daily 1° × 1° gridded precipitation database of rain gauge,](#)

782 [satellite and reanalysis products, Earth Syst. Sci. Data, 11, 1017-1035, 10.5194/essd-11-](#)
783 [1017-2019, 2019.](#)

784 Sakradzija, M., Seifert, A., and Heus, T.: Fluctuations in a quasi-stationary shallow cumulus
785 cloud ensemble, *Nonlin. Processes Geophys.*, 22, 65-85, 10.5194/npg-22-65-2015, 2015.

786 Simmons, A., Uppala, S., Dee, D., and Kobayashi, S.: ERA-Interim: New ECMWF reanalysis
787 products from 1989 onwards, *ECMWF Newsl.*, 110, 1–11, 2007.

788 Stone, D., Risser, M. D., Angelil, O., Wehner, M., Cholia, S., Keen, N., Krishnan, H., Obrien, T.
789 A., and Collins, W. D.: A basis set for exploration of sensitivity to prescribed ocean
790 conditions for estimating human contributions to extreme weather in CAM5.1-1degree,
791 *Weather and climate extremes*, 19, 10-19, 2018.

792

793 [Tang, S., Xie, S., Zhang, Y., Zhang, M., Schumacher, C., Upton, H., Jensen, M. P., Johnson, K.](#)
794 [L., Wang, M., Ahlgrimm, M., Feng, Z., Minnis, P., and Thieman, M.: Large-scale vertical](#)
795 [velocity, diabatic heating and drying profiles associated with seasonal and diurnal variations](#)
796 [of convective systems observed in the GoAmazon2014/5 experiment, Atmos. Chem. Phys.,](#)
797 [16, 14249–14264, https://doi.org/10.5194/acp-16-14249-2016, 2016.](#)

798 Tang, Q., Klein, S. A., Xie, S., Lin, W., Golaz, J.-C., Roesler, E. L., Taylor, M. A., Rasch, P. J.,
799 Bader, D. C., and Berg, L. K.: Regionally refined test bed in E3SM atmosphere model
800 version 1 (EAMv1) and applications for high-resolution modeling, ~~*Geoscientific Model-*~~
801 ~~*Development*~~ *Geosci. Model Dev.*, 12, 2679–2706, <https://doi.org/10.5194/gmd-12-2679->
802 [2019, 2019.](#)

803 ~~(Online), 12, 2019.~~

804 Trenberth, K. E., Zhang, Y., and Gehne, M.: Intermittency in Precipitation: Duration, Frequency,
805 Intensity, and Amounts Using Hourly Data, *Journal of Hydrometeorology*, 18, 1393-1412,
806 10.1175/jhm-d-16-0263.1, 2017.

807 Wang, Y., Liu, X., Hoose, C., and Wang, B.: Different contact angle distributions for
808 heterogeneous ice nucleation in the Community Atmospheric Model version 5,
809 *Atmospheric Chemistry and Physics*, 10411, 2014.

810 Wang, Y., and Zhang, G. J.: Global climate impacts of stochastic deep convection
811 parameterization in the NCAR CAM5, *Journal of Advances in Modeling Earth Systems*, 8,
812 1641-1656, doi:10.1002/2016MS000756, 2016.

813 Wang, Y., Zhang, G. J., and Craig, G. C.: Stochastic convective parameterization improving the
814 simulation of tropical precipitation variability in the NCAR CAM5, *Geophysical Research*
815 *Letters*, 43, 6612-6619, doi:10.1002/2016GL069818, 2016.

816 Wang, Y., Zhang, G. J., and Jiang, Y.: Linking Stochasticity of Convection to Large-Scale
817 Vertical Velocity to Improve Indian Summer Monsoon Simulation in the NCAR CAM5,
818 *Journal of Climate*, 31, 6985-7002, 10.1175/jcli-d-17-0785.1, 2018.

819 [Wang, Y., W. Xia, X. Liu, S. Xie, W. Lin, Q. Tang, H.-Y. Ma, Y. Jiang, B. Wang, and G. J.](#)
820 [Zhang: Disproportionate control on aerosol burden by light rain, *Nature Geoscience*,](#)
821 [<https://doi.org/10.1038/s41561-020-00675-z>, 2021.](#)

822 Watson, P. A. G., Berner, J., Corti, S., Davini, P., Von Hardenberg, J., Sanchez, C., Weisheimer,
823 A., and Palmer, T. N.: The impact of stochastic physics on tropical rainfall variability in
824 global climate models on daily to weekly time scales, *Journal of Geophysical Research*,
825 122, 5738-5762, 2017.

826 Webb, M. J., Andrews, T., Bodas-Salcedo, A., Bony, S., Bretherton, C. S., Chadwick, R.,
827 Chepfer, H., Douville, H., Good, P., and Kay, J. E.: The cloud feedback model
828 intercomparison project (CFMIP) contribution to CMIP6, *Geoscientific Model*
829 *Development*, 2017, 359-384, 2017.

830 Willmott, C. J., and Matsuura, K.: Smart interpolation of annually averaged air temperature in
831 the United States, *Journal of Applied Meteorology*, 34, 2577-2586, 1995.

832 Xie, P., and Arkin, P. A.: Analyses of Global Monthly Precipitation Using Gauge Observations,
833 Satellite Estimates, and Numerical Model Predictions, *Journal of Climate*, 9, 840-858,
834 10.1175/1520-0442(1996)009<0840:AOGMPU>2.0.CO;2, 1996.

835 [Xie, S., R. T. Cederwall, and M. H. Zhang: Developing long-term single-column model/cloud](#)
836 [system-resolving model forcing using numerical weather prediction products constrained by](#)
837 [surface and top of the atmosphere observations. *-J. Geophys. Res.*, 109, -D01104,](#)
838 [\[doi:10.1029/2003JD004045\]\(https://doi.org/10.1029/2003JD004045\), 2004.](#)

839 Xie, S., Lin, W., Rasch, P. J., Ma, P. L., Neale, R., Larson, V. E., Qian, Y., Bogenschutz, P. A.,
840 Caldwell, P., and Cameron - Smith, P.: Understanding cloud and convective characteristics
841 in version 1 of the E3SM atmosphere model, *Journal of Advances in Modeling Earth*
842 *Systems*, 10, 2618-2644, 2018.

843 Xie, S., Wang, Y., Lin, W., Ma, H., Tang, Q., Tang, S., Zheng, X., Golaz, J., Zhang, G. J., and
844 Zhang, M.: Improved Diurnal Cycle of Precipitation in E3SM With a Revised Convective

845 Triggering Function, *Journal of Advances in Modeling Earth Systems*, 11, 2290-2310,
846 2019.

847 Zhang, G. J., and Mu, M.: Simulation of the Madden–Julian Oscillation in the NCAR CCM3
848 Using a Revised Zhang–McFarlane Convection Parameterization Scheme, *Journal of*
849 *Climate*, 18, 4046-4064, 2005a.

850 Zhang, G. J., and Mu, M.: Effects of modifications to the Zhang-McFarlane convection
851 parameterization on the simulation of the tropical precipitation in the National Center for
852 Atmospheric Research Community Climate Model, version 3, *Journal of Geophysical*
853 *Research: Atmospheres*, 110, D09109, 10.1029/2004JD005617, 2005b.

854 Zhang, G. J., Song, X., and Wang, Y.: The double ITCZ syndrome in GCMs: A coupled
855 feedback problem among convection, clouds, atmospheric and ocean circulations,
856 *Atmospheric Research*, 2019.

857 Zhang, G. J., and Wang, H.: Toward mitigating the double ITCZ problem in NCAR CCSM3,
858 *Geophysical Research Letters*, 33, 2006.

859 Zhang, Y., Xie, S., Lin, W., Klein, S. A., Zelinka, M., Ma, P. L., Rasch, P. J., Qian, Y., Tang, Q.,
860 and Ma, H. Y.: Evaluation of clouds in version 1 of the E3SM atmosphere model with
861 satellite simulators, *Journal of Advances in Modeling Earth Systems*, 11, 1253-1268, 2019.
862

863

Table captions

864

Table 1. List of simulations.

865

866 **Table captions:**

867

868 **Table 1.** List of simulations.

Simulation	Years	Vertical Levels	Description
EAMv1	6	72	Standard EAMv1 with the default deterministic ZM deep convection scheme for simulating the current climate ¹
STOCH	6	72	Same as EAMv1, but coupling with the PC stochastic deep convection scheme with the deterministic ZM deep convection scheme
EAMv1-30L	6	30	Same as EAMv1, but using a vertical resolution configuration of 30 layers
STOCH-30L	6	30	Same as STOCH, but using a vertical resolution configuration of 30 layers
EAMv1-4K	3	72	Same as EAMv1, but for simulating a warmer world ²
STOCH-4K	3	72	Same as STOCH, but for simulating a warmer world

869 ¹Atmosphere-only simulations, using fully prognostic atmosphere and land models with
 870 prescribed, seasonally varying climatological present-day sea surface temperatures (SSTs) and
 871 sea ice extent, recycled yearly.

872 ²For simulating a warmer world, the atmosphere-only simulations are subjected to a composite
 873 SST warming pattern derived from the Coupled Model Intercomparison Project Phase 3
 874 (CMIP3) coupled models.

875

876 **Figure captions**

877 **Figure 1.** Spatial distributions of the 20–80 day variance of rainfall from (a) the Xie-Arkin
878 observations, (b) TRMM, (c) EAMv1, and (d) STOCH, respectively (units: $\text{mm}^2 \text{d}^{-2}$).

879 **Figure 2.** Spatial distributions of the synoptic variance of rainfall from (a) TRMM, (b) EAMv1,
880 and (c) STOCH, respectively (units: $\text{mm}^2 \text{d}^{-2}$).

881 **Figure 3.** Frequency distributions of (a) total (solid line), (b) convective (solid line) and large-
882 scale (dashed line) precipitation intensity over the tropics (20°S , 20°N) for EAMv1 (blue) and
883 STOCH (red) respectively. For total precipitation, the TRMM observations (black) and ensemble
884 mean of multiple observations (Obs. ens, purple) where each observation is denoted by the gray
885 line are included for evaluation.

886 **Figure 4.** Frequency distributions of total precipitation intensity over Amazon (20°S - 5°N , 40°W -
887 80°W), tropical western Pacific (TWP) (0°N - 15°N , 130°E - 170°E), India (14°N - 26.5°N , 74.5°E -
888 94°E ; for June-September), Maritime Continent (MC) (10°S - 10°N , 90°E - 160°E), Southern Great
889 Plains (SGP) (37°N - 42°N , 90°W - 110°W ; for May-August) and eastern China (25°N - 35°N ,
890 100°E - 120°E ; for June-August) for TRMM (black), EAMv1 (blue) and STOCH (red)
891 respectively.

892 **Figure 5.** Spatial distributions of frequencies of total rainfall intensity larger than (top row) 1
893 mm d^{-1} , (middle row) between 1 and 20 mm d^{-1} and (bottom row) larger than 20 mm d^{-1} for
894 TRMM, EAMv1 and STOCH, respectively.

895 **Figure 6.** Annual mean rainfall amount distributions of (a) total precipitation (solid line) over the
896 tropics (20°S , 20°N) for GPCP 1DD (grey), TRMM (black), EAMv1 (blue) and STOCH (red),
897 respectively. Individual distributions of (b) convective (solid line) and large-scale (dashed line)
898 precipitation in EAMv1 (blue) and STOCH (red) are also shown. The rainfall intensity on the x-
899 axis is on a logarithmic scale with bin intervals of $\Delta \ln(R) = \Delta R/R = 0.1$.

900 **Figure 7.** Histogram of percentage frequency of total rainy events as a function of their duration
901 using 3-hourly data (conditional probability of rainfall, given rainfall the previous times) from
902 TRMM (black), EAMv1 (blue) and STOCH (red) for the threshold rainfall rate of 1 mm d^{-1} over
903 the tropics.

904 **Figure 8.** Same as Fig. 3, but including PDFs for EAMv1-30L and STOCH-30L (both dashed
905 lines).

906 **Figure 9.** Joint PDFs of CAPE versus convective precipitation over the tropics (20°S , 20°N)
907 from (a) EAMv1, (b) EAMv1-30L, (c) STOCH, and (d) STOCH-30L, respectively.

908 **Figure 10.** Scatterplots of total precipitation versus CAPE at the ARM (a-c) SGP and (d-f)
909 Amazon sites for (a & d) observations calculated from multi-year sounding data (2014-2015 for
910 Amazon and 2004-2018 for SGP), (b & e) EAMv1 and (c & f) STOCH.~~Scatterplots of total~~
911 ~~precipitation versus CAPE at the ARM (a, c & e) SGP and (b, d & f) Amazon sites for (a & b)~~
912 ~~observations calculated from multi year sounding data (2014 2015 for Amazon and 2004 2018~~
913 ~~for SGP), (c & d) EAMv1 and (e & f) STOCH.~~Frequencies of the resolved upward moisture flux
914 over the tropics (20°S, 20°N) in EAMv1, EAMv1 30L, STOCH and STOCH 30L, respectively.

915 **Figure 11.** Global distributions of total precipitation for (a) GPCP, (b) EAMv1, and (c) STOCH,
916 and differences of (d) total, (e) convective and (f) large-scale precipitation between STOCH and
917 EAMv1. Differences with a confidence level greater than 95% in (d-f) are stippled.

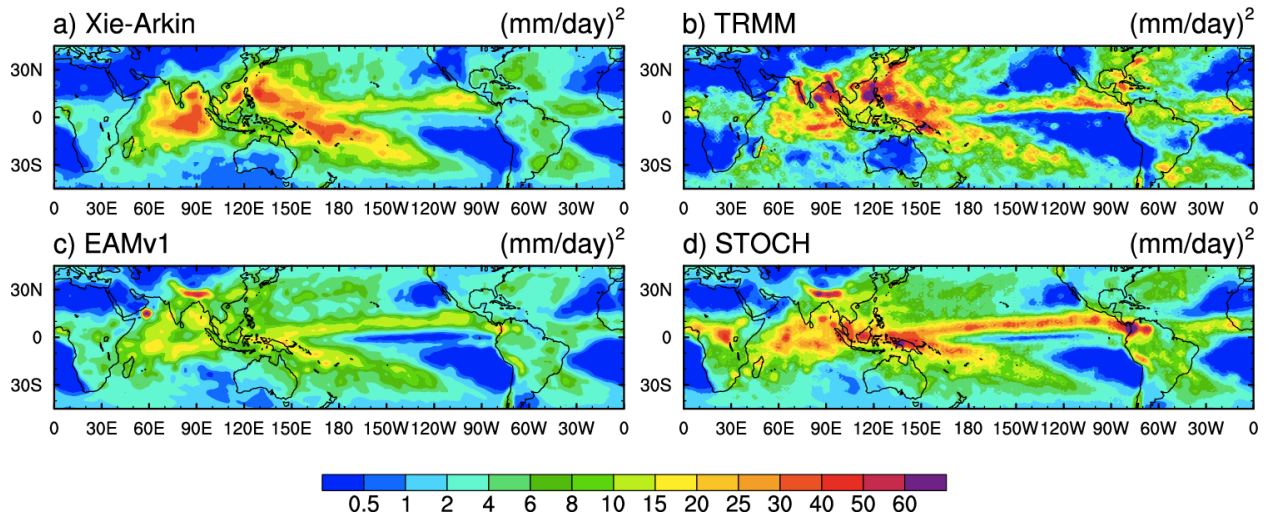
918 **Figure 12.** Annual and zonal mean cross sections of (a-c) temperature and (d-f) specific
919 humidity for (a & d) ERAI and differences for (b & e) EAMv1-ERAI and (c & f) STOCH-
920 EAMv1. Differences with a confidence level greater than 95% in between STOCH and EAMv1
921 are stippled.

922 **Figure 13.** Taylor diagram with metrics for STOCH, compared with EAMv1.

923 **Figure 14.** Geographical distributions of responses of (a & b) annual mean precipitation, (c & d)
924 the coefficient a , and (e & f) the fractional change in precipitation extremes (R95p) to climate
925 warming from +4K experiments. Differences with a confidence level greater than 95% are
926 stippled.~~Geographical distributions of responses of (a&b) annual mean precipitation and (c&d)~~
927 ~~precipitation extremes (R95p) to climate warming from +4K experiments. Differences with a~~
928 ~~confidence level greater than 95% are stippled.~~

929

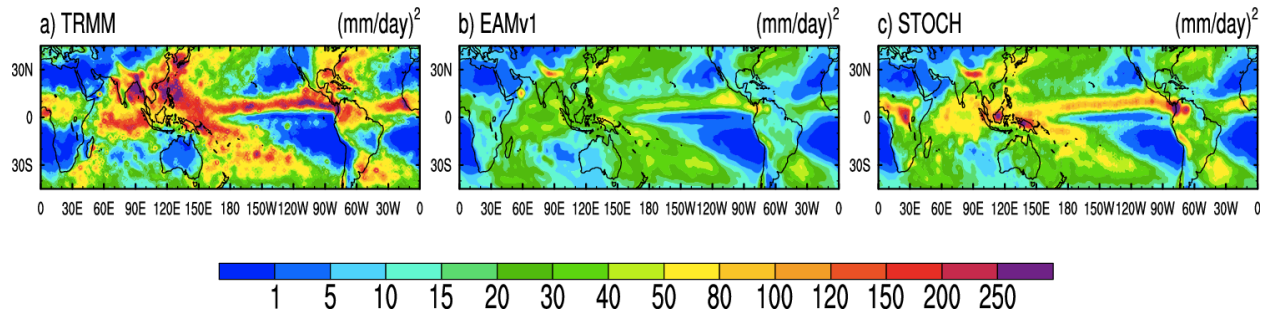
930 **Figures**



931

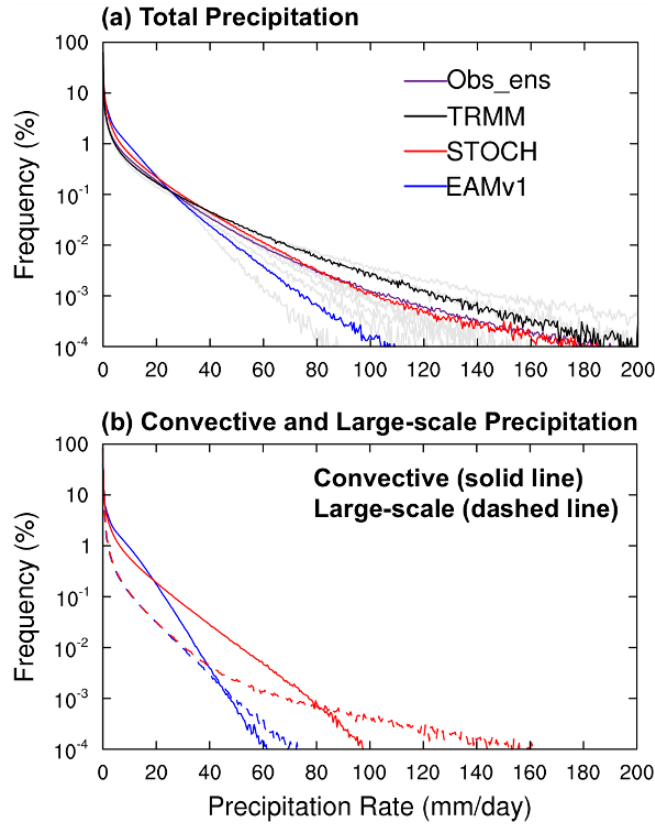
932 **Figure 1.** Spatial distributions of the 20–80 day variance of rainfall from (a) the Xie-Arkin
933 observations, (b) TRMM, (c) EAMv1, and (d) STOCH, respectively (units: $\text{mm}^2 \text{d}^{-2}$).

934

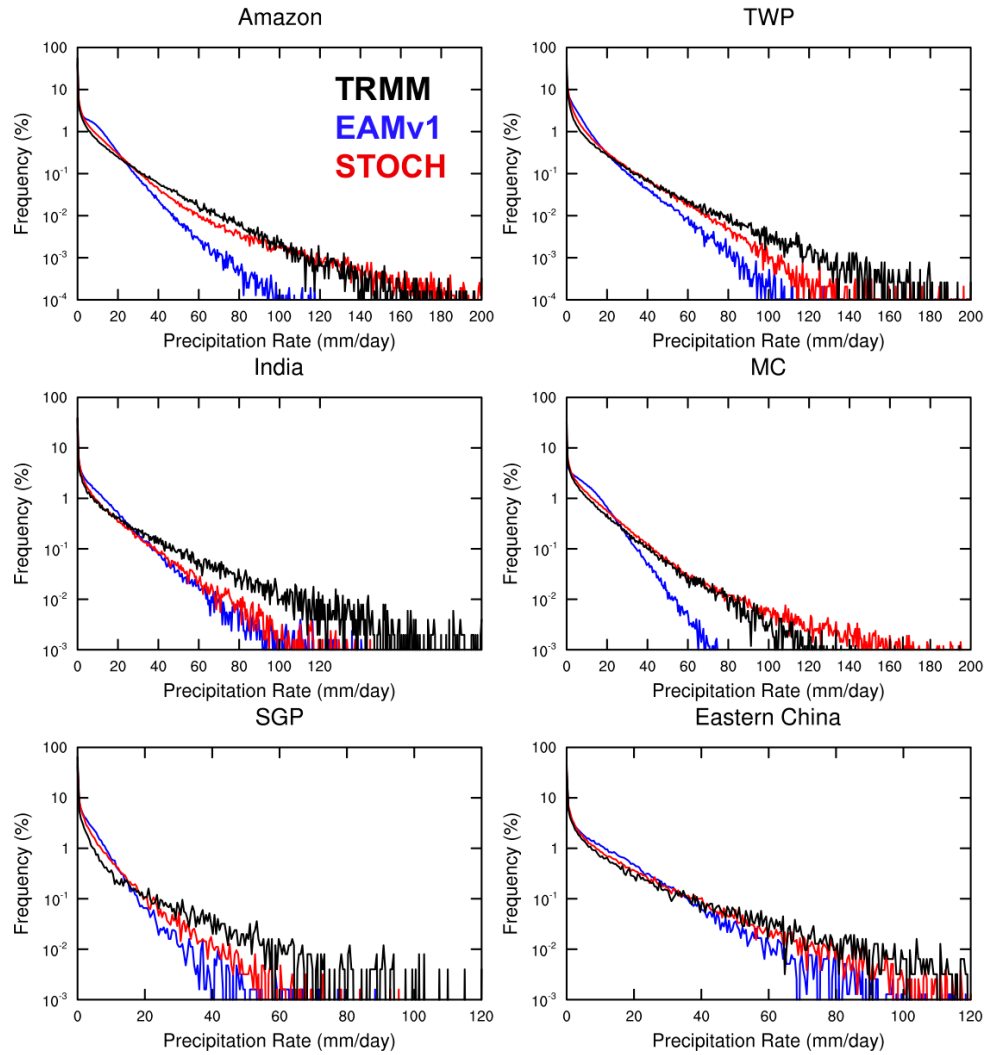


935

936 **Figure 2.** Spatial distributions of the synoptic variance of rainfall from (a) TRMM, (b) EAMv1,
 937 and (c) STOCH, respectively (units: $\text{mm}^2 \text{d}^{-2}$).
 938



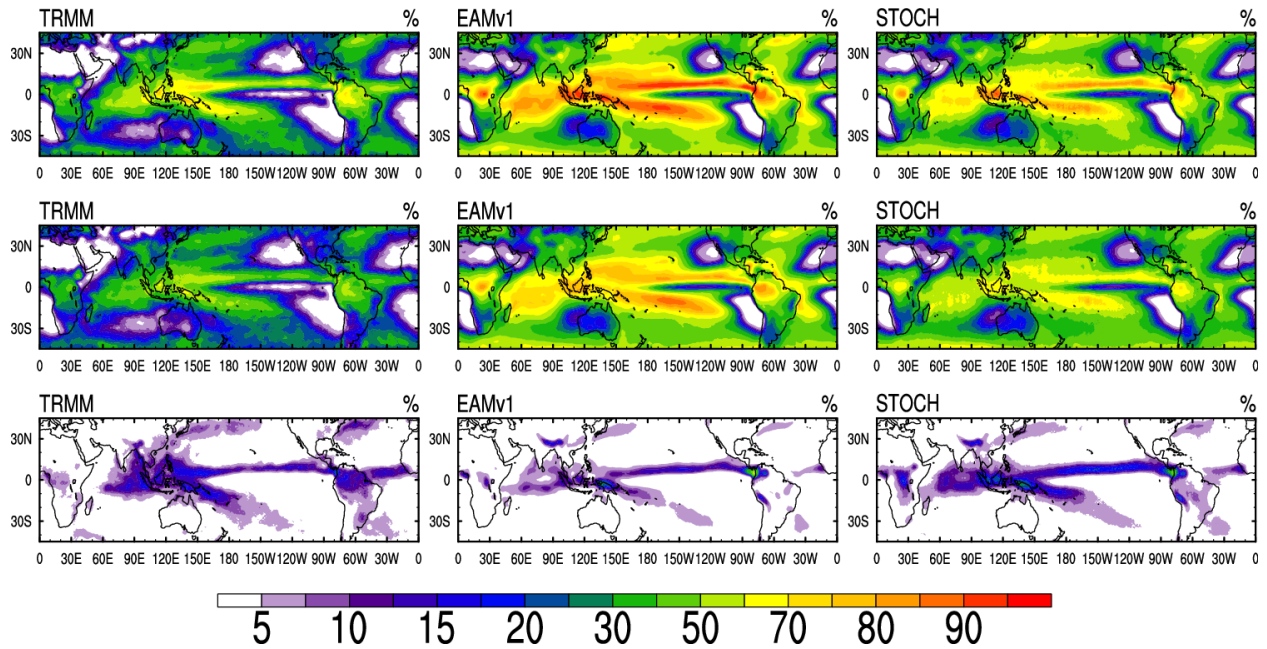
939
 940 **Figure 3.** Frequency distributions of (a) total (solid line), (b) convective (solid line) and large-
 941 scale (dashed line) precipitation intensity over the tropics (20°S, 20°N) for EAMv1 (blue) and
 942 STOCH (red) respectively. For total precipitation, the TRMM observations (black) and ensemble
 943 mean of multiple observations (Obs_ens, purple) where each observation is denoted by the gray
 944 line are included for evaluation.
 945



946

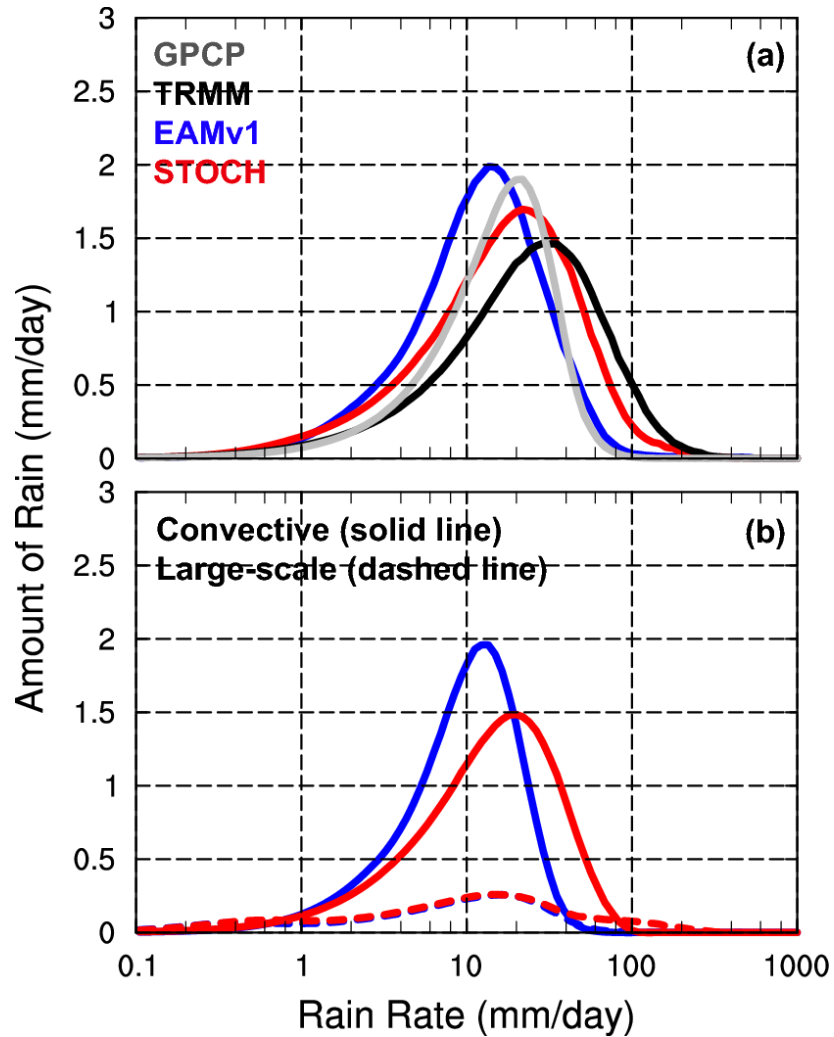
947 **Figure 4.** Frequency distributions of total precipitation intensity over Amazon (20°S-5°N, 40°W-
 948 80°W), tropical western Pacific (TWP) (0°N-15°N, 130°E-170°E), India (14°N-26.5°N, 74.5°E-
 949 94°E; for June-September), Maritime Continent (MC) (10°S-10°N, 90°E-160°E), Southern Great
 950 Plains (SGP) (37°N-42°N, 90°W-110°W; for May-August) and eastern China (25°N-35°N,
 951 100°E-120°E; for June-August) for TRMM (black), EAMv1 (blue) and STOCH (red)
 952 respectively.

953



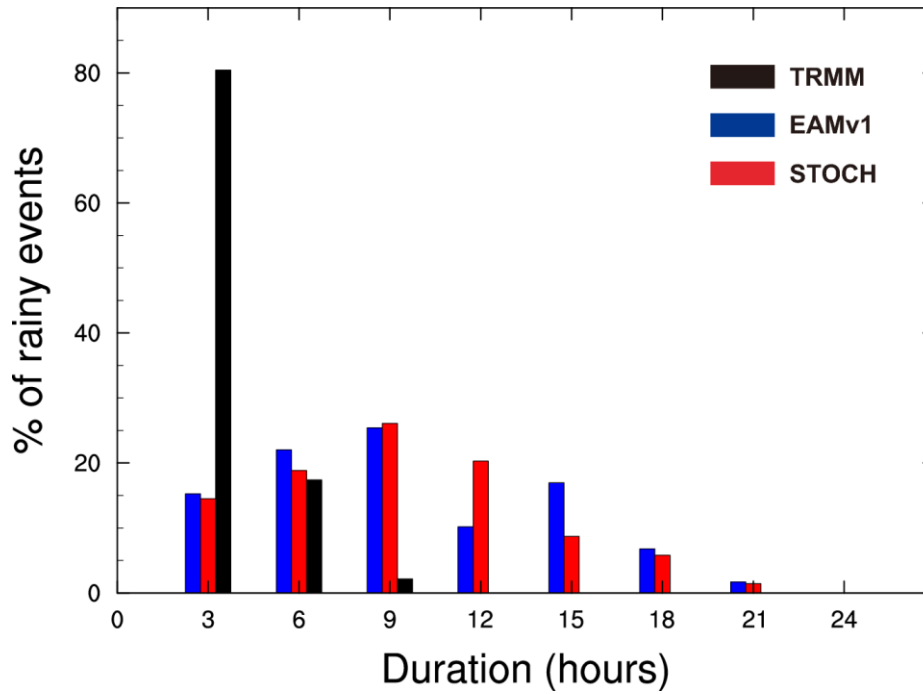
954

955 **Figure 5.** Spatial distributions of frequencies of total rainfall intensity larger than (top row) 1
 956 mm d⁻¹, (middle row) between 1 and 20 mm d⁻¹ and (bottom row) larger than 20 mm d⁻¹ for
 957 TRMM, EAMv1 and STOCH, respectively.
 958



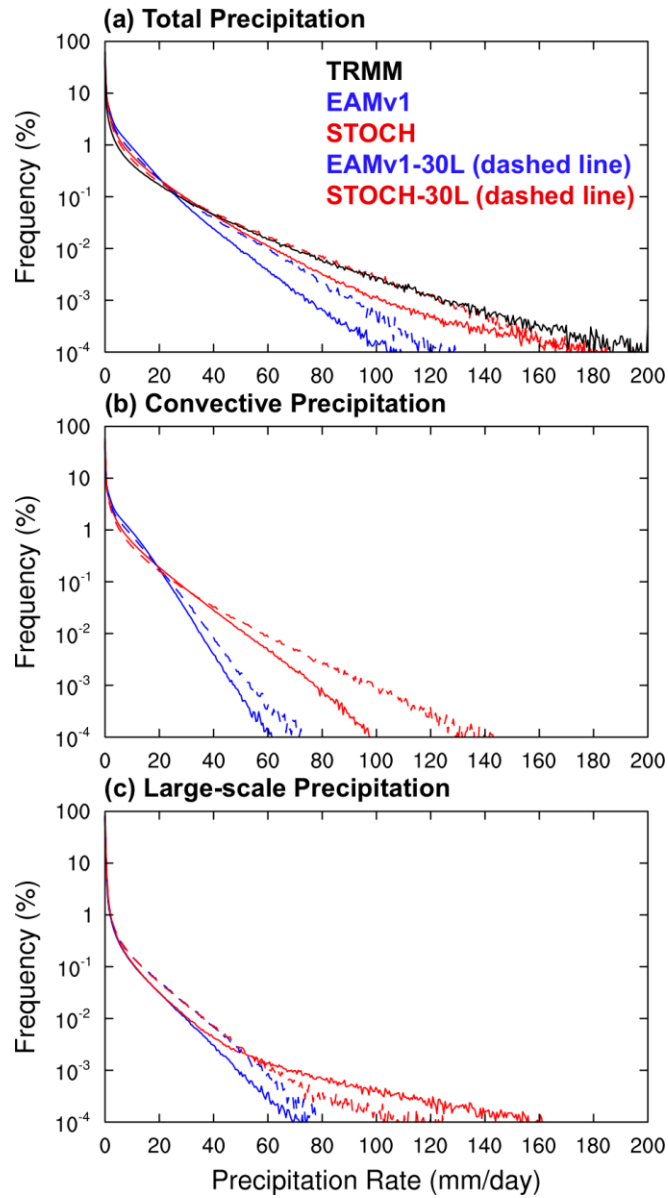
959
 960
 961
 962
 963
 964
 965

Figure 6. Annual mean rainfall amount distributions of (a) total precipitation (solid line) over the tropics (20°S, 20°N) for GPCP 1DD (grey), TRMM (black), EAMv1 (blue) and STOCH (red), respectively. Individual distributions of (b) convective (solid line) and large-scale (dashed line) precipitation in EAMv1 (blue) and STOCH (red) are also shown. The rainfall intensity on the x-axis is on a logarithmic scale with bin intervals of $\Delta \ln(R) = \Delta R/R = 0.1$.



966
 967
 968
 969
 970
 971

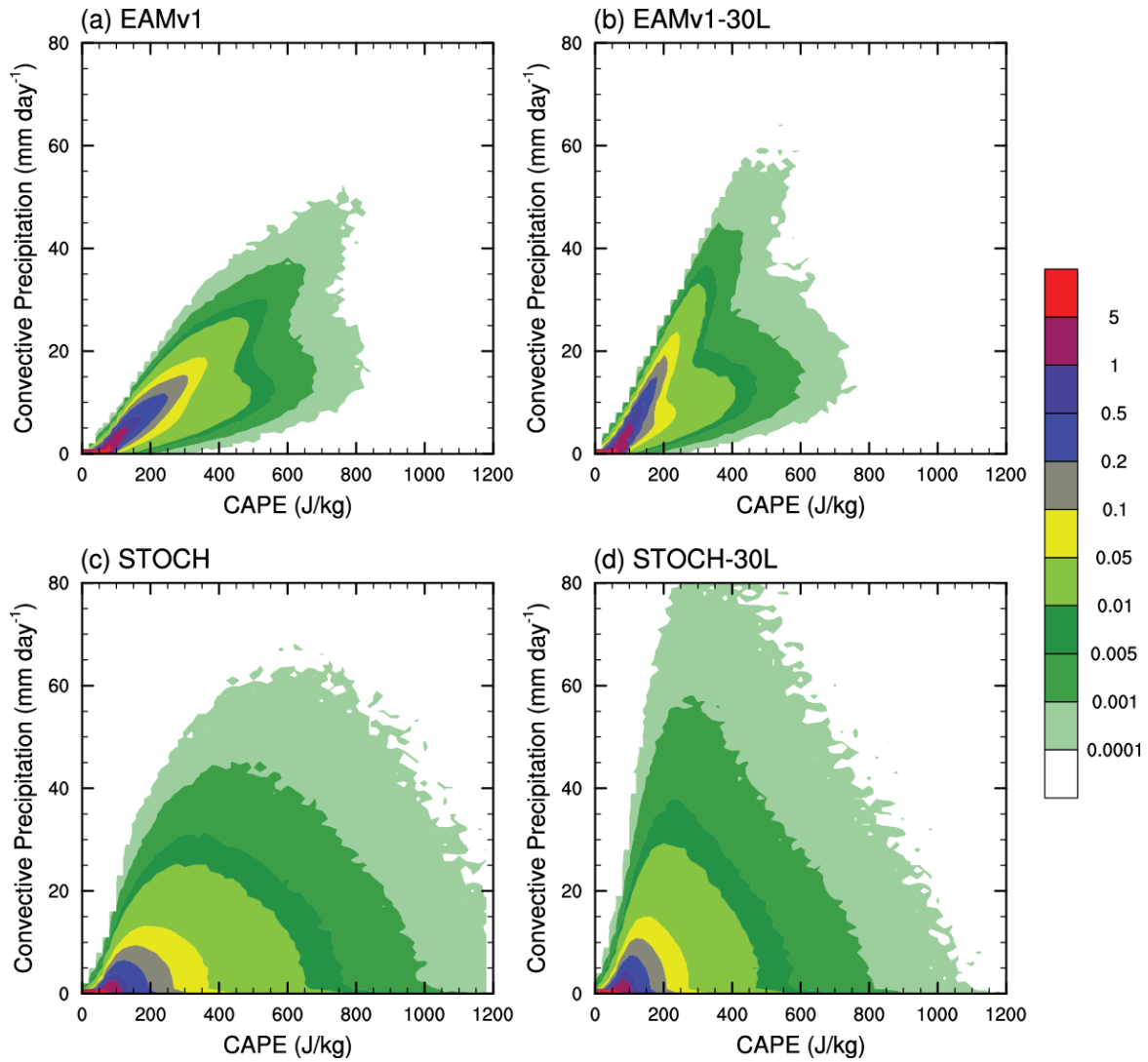
Figure 7. Histograms of percentage frequency of total rainy events as a function of their duration using 3-hourly data (conditional probability of rainfall, given rainfall the previous times) from TRMM (black), EAMv1 (blue) and STOCH (red) for the threshold rainfall rate of 1 mm d⁻¹ over the tropics.



972

973 **Figure 8.** Same as Fig. 3, but including PDFs for EAMv1-30L and STOCH-30L (both dashed
 974 lines).

975

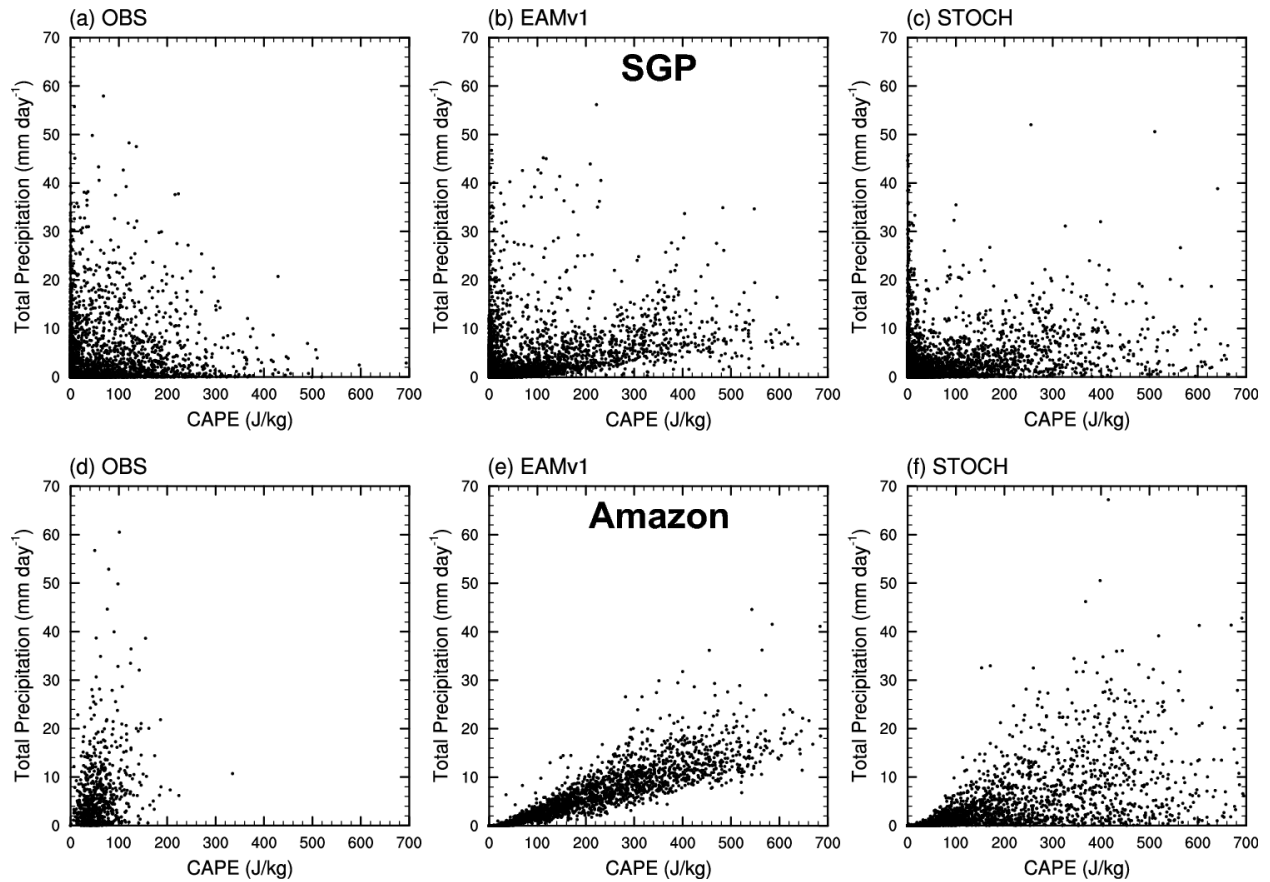


976

977 **Figure 9.** Joint PDFs of CAPE versus convective precipitation over the tropics (20°S, 20°N)

978 from (a) EAMv1, (b) EAMv1-30L, (c) STOCH, and (d) STOCH-30L, respectively.

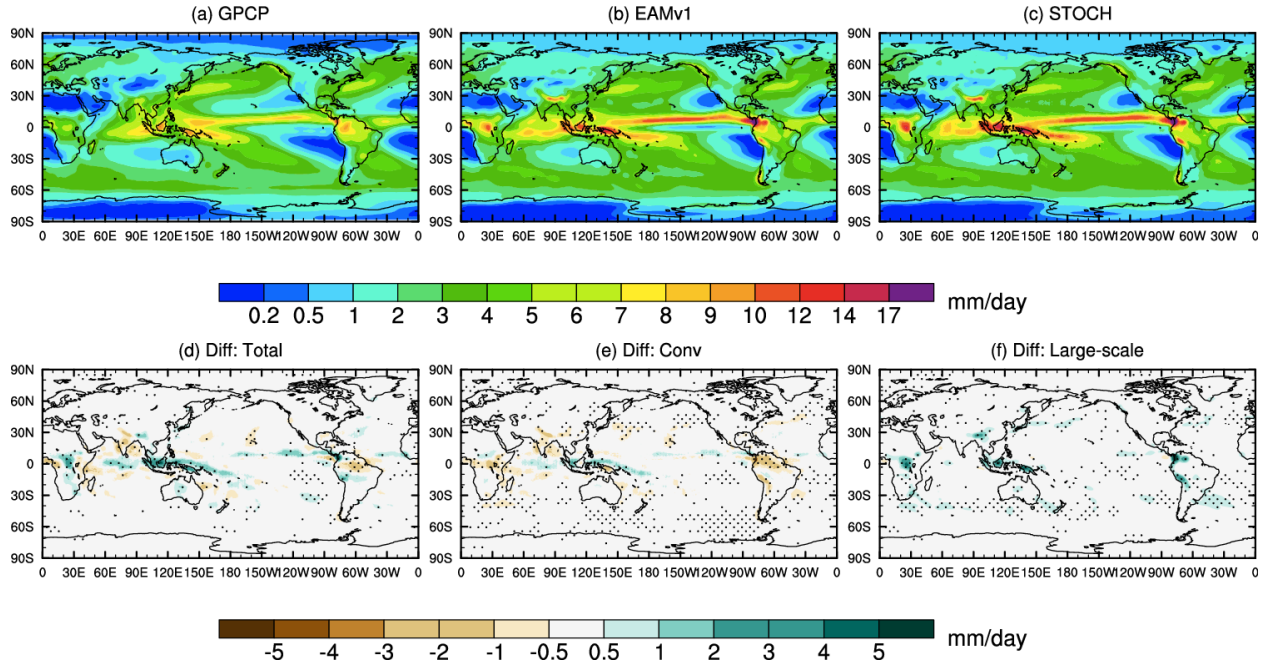
979



980

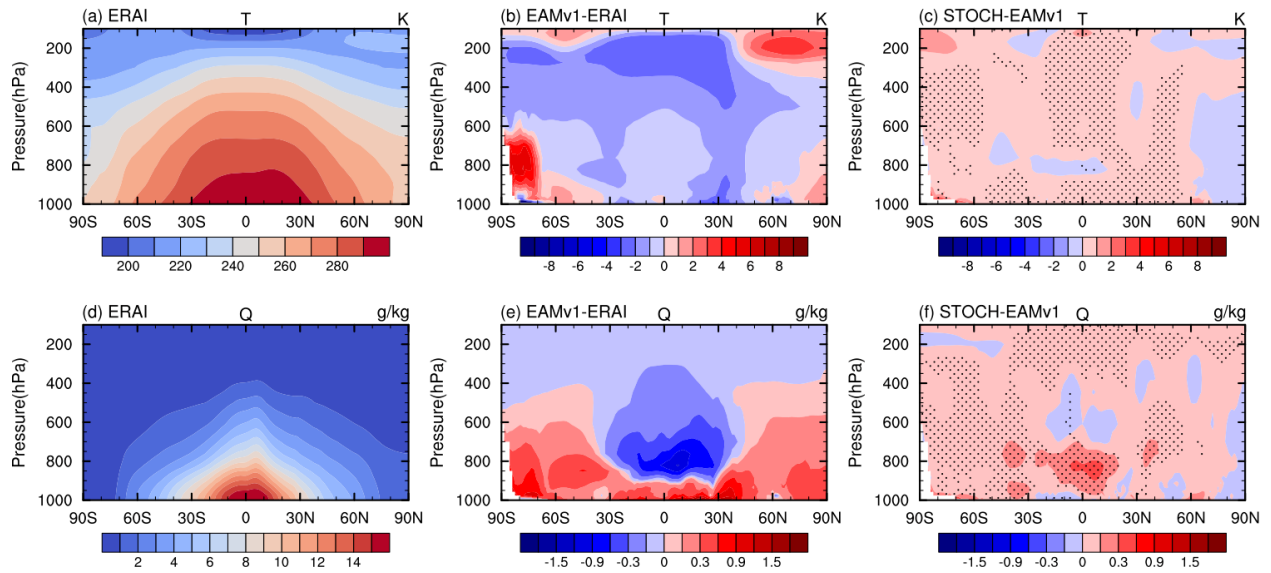
981 **Figure 10.** Scatterplots of total precipitation versus CAPE at the ARM (a, c, e & e) SGP and (d-
 982 ~~fb, d & f~~) Amazon sites for (a & ~~db~~) observations calculated from multi-year sounding data
 983 (~~2014-2015 for Amazon and 2004-2018 for SGP~~), (~~be & ed~~) EAMv1 and (~~ce & f~~)
 984 ~~STOCH~~. Frequencies of the resolved upward moisture flux over the tropics (20oS, 20oN) in
 985 ~~EAMv1, EAMv1-30L, STOCH and STOCH-30L, respectively.~~

986



987
 988
 989
 990
 991

Figure 11. Global distributions of total precipitation for (a) GPCP, (b) EAMv1, and (c) STOCH, and differences of (d) total, (e) convective and (f) large-scale precipitation between STOCH and EAMv1. Differences with a confidence level greater than 95% in (d-f) are stippled.



992

993

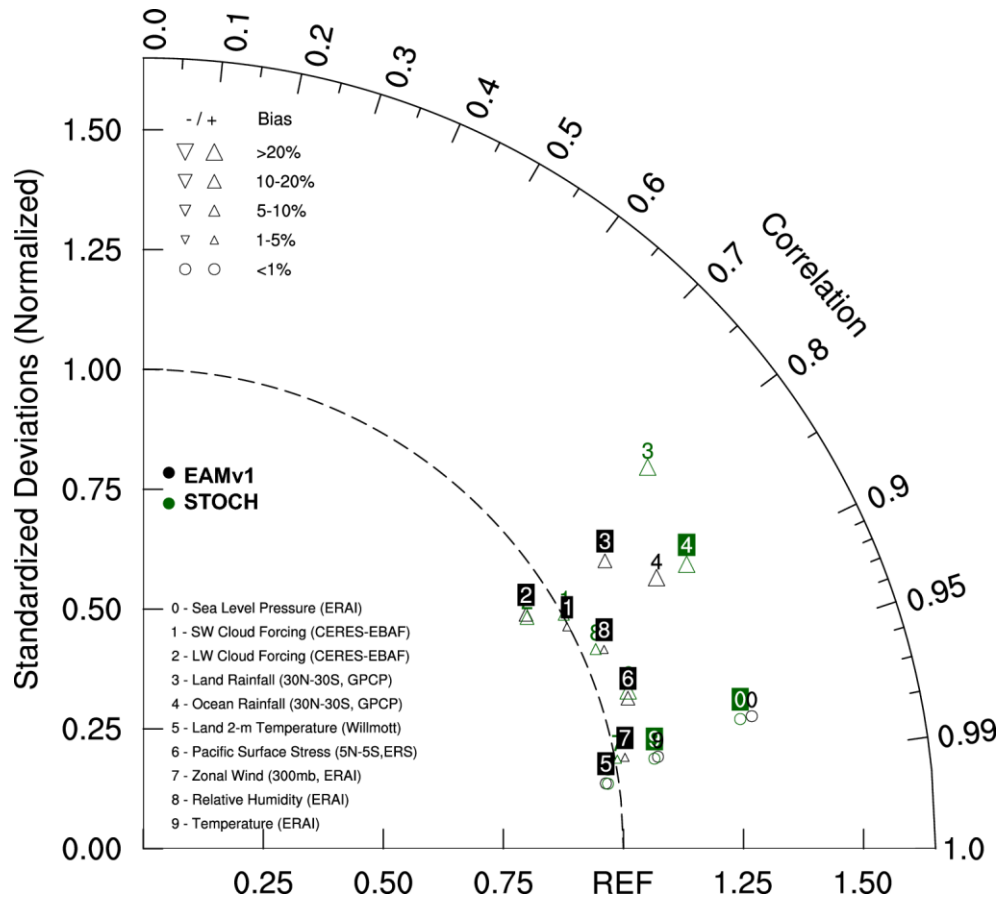
994

995

996

997

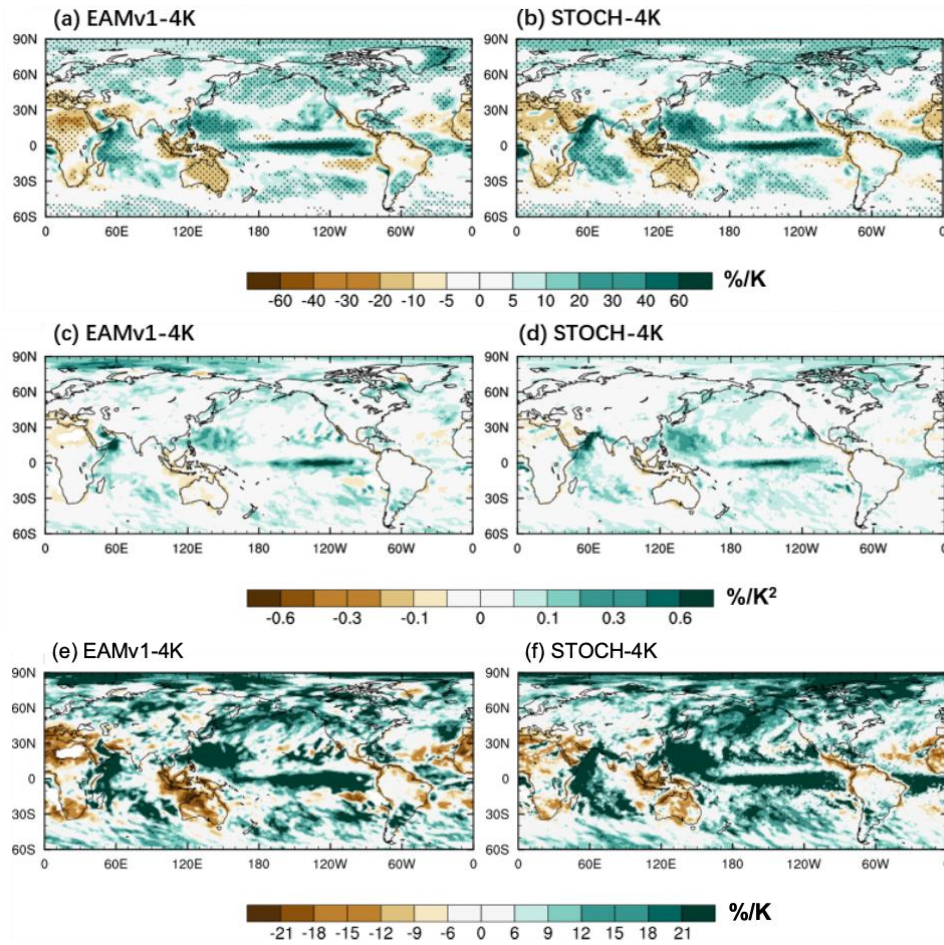
Figure 12. Annual and zonal mean cross sections of (a-c) temperature and (d-f) specific humidity for (a & d) ERAI and differences for (b & e) EAMv1-ERAI and (c & f) STOCH-EAMv1. Differences with a confidence level greater than 95% in between STOCH and EAMv1 are stippled.



998

999 **Figure 13.** Taylor diagram with metrics for STOCH, compared with EAMv1.

1000



1001
 1002 **Figure 14.** Geographical distributions of responses of (a & b) annual mean precipitation, and (c
 1003 & d) the coefficient of precipitation extremes (R95p), and (e & f) the fractional change in
 1004 precipitation extremes (R95p) to climate warming from +4K experiments. Differences with a
 1005 confidence level greater than 95% are stippled.